Topology optimization for fluid flow devices modeled through the Multiple Reference Frame approach

Diego Hayashi Alonso[a], Emílio Carlos Nelli Silva[a,*]

[a] *Department of Mechatronics and Mechanical Systems Engineering, Polytechnic School of the University of São Paulo, SP, Brazil, Av. Prof. Mello Moraes, 2231 - 05508-030, São Paulo, Brazil.*

Abstract

Fluid flow devices have been algorithmically designed through optimization methods, and this task is relatively complex for flow machines. Particularly, one recent development is the use of the topology optimization method for this task, which is capable of achieving possibly non-intuitive geometries and even auxiliary structures, such as splitter blades without ever imposing it as a condition for the design. The design of the rotating part of the rotor has already been previously considered. However, in the presence of stationary parts surrounding the rotor, such as diffuser blades, the fluid flow behavior may change, meaning that it may be interesting to consider this different dynamic in the design. One possible approach for this is the Multiple Reference Frame approach, which considers the fluid flow dynamics inside the rotor being computed in the rotating reference frame, whilst the fluid flow dynamics outside the rotor is being computed in the stationary reference frame. In particular, this implies the need for some changes in the topology optimization formulation, also impacting the choice of objective functions. Therefore, here the topology optimization method is formulated for the MRF approach, and a new combination for the multi-objective function is proposed. The discrete design variable configuration from the Topology Optimization of Binary Structures approach is adopted with some adjustments to account for the MRF approach. The fluid flow is chosen to be laminar or turbulent. Numerical examples are presented in 2D for the rotor-diffuser in order to consider some aspects that affect the overall topology optimization design.

Keywords: Fluid topology optimization, Multiple Reference Frame, Frozen rotor, Impeller-diffuser, Turbulence, Automatic differentiation

1. Introduction

There are various optimization approaches that can be used for improving the performance of fluid flow devices. One approach that has been gaining momentum is the use of the topology optimization method for fluid flows [1], which has already been considered for various different flow physics (Navier-Stokes flows [2], non-Newtonian flows [3], turbulent flows [4], thermal-fluid flows [5], compressible flows [6] etc.), various different fluid flow devices (mixers [7], rectifiers [8], bladed rotors [9], arterial by-pass grafts [10], fluid diodes [11] etc.) and various different implementation approaches (pseudo-density [1], level-set [12], topological derivatives [13]). Essentially, fluid flow topology optimization consists of distributing fluid and solid along a given domain, in order to obtain the positions and shapes of the necessary solid structures that lead to an optimized fluid flow path according to given requirements and objectives. For example, when tackling topology optimization *for* flow machines [9], it is important to improve their performance and efficiency from the fluid flow point-of-view. While increasing the complexity and range of applications of fluid flow topology optimization, one may undoubtedly stumble across turbulence [4], which has already been considered in topology optimization for various Reynolds Averaged Navier-Stokes (RANS) models, such as the Spalart-Allmaras model [4, 14], the k-ω model [15], the k-ε model [16], and the Wray-Agarwal (2018) model [17]. The Wray-Agarwal (2018) model [18], also referred to as WA2018, is a single-equation turbulence model that does not explicitly depend on the wall distance, eases the choice and reduces the quantity of parameters for the topology optimization process [17], and is competitive with the SST k-ω model [19].

When considering rotating parts in topology optimization, such as the rotor of a flow machine, the fluid flow equations should be solved inside a rotating reference frame [9]. However, the 2D swirl flow model (2D axisymmetric flow model with rotation around an axis) does not have this strict requirement. This is because the axisymmetry hypothesis makes both stationary and rotating reference frame equations equivalent except for a conversion between velocities (absolute and relative). This enables performing topology optimization considering stationary

*Corresponding author. Tel.: +55 11 3091 9754; fax: +55 11 3091 5722.

Email address: ecnsilva@usp.br (Emílio Carlos Nelli Silva)

Published article (Published in its final form: June, 2023):
Alonso, D.H. & Silva, E.C.N. **Topology optimization for fluid flow devices modeled through the Multiple Reference Frame approach.** Applied Mathematical Modelling 118, 592–617 (2023). https://doi.org/10.1016/j.apm.2023.01.019

and rotating parts [20–22] while taking into account the same fluid flow equations inside the entire design domain, needing only to care about the distance between the rotating and stationary parts, in order to avoid undesirable contact. However, other types of fluid flow devices (2D/3D) do not feature such convenient hypothesis (axisymmetry), meaning that the fluid flow equations should be treated differently for the rotating blades and the stationary parts, and there is also the inherent necessity to avoid the collision of the blades and the stationary parts, as opposed to just contact between them, as in the 2D swirl flow model. Therefore, a new approach is required for the topology optimization of non-axisymmetric fluid flow devices.

In Computational Fluid Dynamics (CFD), the first approach that comes to mind when dealing with rotating and stationary parts is to consider a transient simulation (sliding mesh model) [23]. However, the computational cost of considering transience is high due to the large amount of short time steps that is required [24], and is worsened when considering topology optimization, which would require repeating the entire simulation multiple times, at each topology optimization iteration. Thus, when the fluid flow is expected to reach a continuous operation condition, two approaches may be considered for an approximated steady-state simulation: Multiple Reference Frame (MRF) [25] and mixing plane [26]. The MRF approach, also referred to as the *frozen rotor* approach, consists of defining a cylinder that encompasses all of the rotating parts, and solving the rotating fluid flow equations only inside this cylinder, leaving the outside to the stationary fluid flow equations. Thus, this steady-state approximation *freezes* the positions of the rotor blades, while assuming the rotating effect on the fluid around them. The other approach (mixing plane) consists of performing the same as the MRF approach; however, an averaging is performed on the interface between the rotating and stationary domains. There are various approaches for this averaging, such as area- and flow rate-based. Thus, there would be two extrema: the MRF approach, which considers local effects of the blades inside the rotating zone, and the mixing plane approach, which considers the average effects of the blades. As a matter of fact, when under 2D incompressible flow, the mixing plane approach decouples the fluid flow physics from both domains, which means that the design could be considered separately for the stationary [27] and rotating [9] parts of the flow machine. The same is not valid for the MRF approach, and the present work will focus on extending the topology optimization formulation for fluid flow devices to it, which results in a unique topology optimization formulation in the sense that a unified formulation can be derived and elaborated for the whole design domain. According to Elder et al. [24], the MRF approach is robust and features no additional difficulties for performing the simulation; however, the interpretation of the results may become more difficult. Moreover, CFD simulations using MRF have various interesting applications, such as impeller-diffuser configurations [24], mixing vessels [28] and cooling fans [29], and CFD implementations are available in various CFD softwares, such as Ansys Fluent® , OpenFOAM® , COMSOL® etc. Although still not in topology optimization, there are several works considering parametric [30], and shape optimizations [31].

Thus, this work presents the topology optimization formulation for fluid flow devices through the MRF approach, for the cases of either laminar or turbulent flows. The turbulent model being used is WA2018 [17, 18]. The optimization algorithm is the Topology Optimization of Binary Structures (TOBS) algorithm [32, 33], which is extended to to be subdomain-aware, the design variable is nodal, and the material model is the traditional one presented in Borrvall and Petersson [1]. The fluid flow equations are implemented in the FEniCS platform [34], while the sensitivities are computed from the adjoint method [35]. Due to convergence issues when considering turbulence, the efficient CFD platform OpenFOAM® [36], which is not capable of automatically deriving the adjoint model, is used for the simulations, through the FEniCS TopOpt Foam library [37]. The resulting adjoint model is solved through the unsymmetric sparse linear solver UMFPACK [38].

This paper is organized as follows: in Section 2, the MRF formulation is presented for laminar and turbulent flows; in Section 3, the topology optimization formulation is presented; in Section 4, the numerical implementation is described; in Section 5, some numerical results are presented; and in Section 6, some conclusions are inferred.

2. MRF formulation

In order to present the MRF formulation, it is first necessary to present the fluid flow formulations in the stationary (absolute) and rotating (relative) reference frames. The basic fluid flow equations consist of the linear momentum (Navier-Stokes) and continuity equations, which are initially presented for laminar flow. In this case, the flow is assumed to be under steady-state regime and the fluid is incompressible. Therefore, based on Romero and Silva [9],

- Stationary reference frame:

$$\begin{aligned} &\nabla \bullet \boldsymbol{v}_{\text{abs}} = 0, \text{ and} \\ &\rho \nabla \boldsymbol{v}_{\text{abs}} \bullet \boldsymbol{v}_{\text{abs}} = \nabla \bullet \boldsymbol{T} + \rho \boldsymbol{f} + \boldsymbol{f}_{r,s}(\alpha); \end{aligned} \tag{1}$$

- Rotating reference frame:

$$\begin{aligned} &\nabla \bullet \boldsymbol{v} = 0, \text{ and} \\ &\rho \nabla \boldsymbol{v} \bullet \boldsymbol{v} = \nabla \bullet \boldsymbol{T} + \rho \boldsymbol{f} - 2\rho(\boldsymbol{\omega} \wedge \boldsymbol{v}) - \rho \boldsymbol{\omega} \wedge (\boldsymbol{\omega} \wedge \boldsymbol{r}) + \boldsymbol{f}_{r,r}(\alpha); \end{aligned} \tag{2}$$

where $\boldsymbol{v}_{\text{abs}}$ is the absolute velocity, $\boldsymbol{v}$ is the relative velocity, p is the pressure, ρ is the density, μ is the dynamic viscosity, $\rho \boldsymbol{f}$ is a body force acting on the fluid per unit volume (for completeness), $\boldsymbol{\omega} = (0, 0, \omega_0)$ is the rotation vector, $-2\rho(\boldsymbol{\omega} \wedge \boldsymbol{v})$ and $-\rho \boldsymbol{\omega} \wedge (\boldsymbol{\omega} \wedge \boldsymbol{r})$ are the inertial forces

($\wedge$ denotes cross product), and $\boldsymbol{r}$ is the radial coordinate ($r = \sqrt{x^2 + y^2}$). The additional force term that is used in topology optimization to model the solid material, is divided into $\boldsymbol{f}_{r,s}(\alpha)$, for the stationary part, and $\boldsymbol{f}_{r,r}(\alpha)$, for the rotating part, where α is the design variable for topology optimization (*pseudo-density*). The stress tensor ($\boldsymbol{T}$) is the fluid stress tensor, which is the same for both reference frames, and can be defined as

$$\boldsymbol{T} = 2\mu\boldsymbol{\epsilon} - p\boldsymbol{I} \ , \ \boldsymbol{\epsilon} = \frac{1}{2}(\nabla\boldsymbol{v} + \nabla\boldsymbol{v}^T). \tag{3}$$

In order to combine both equations for, e.g. the absolute velocity $\boldsymbol{v}_{\text{abs}}$, it is first necessary to convert the equations of the rotating reference frame from $\boldsymbol{v}$ to $\boldsymbol{v}_{\text{abs}}$, through the relation $\boldsymbol{v}_{\text{abs}} = \boldsymbol{v} + \boldsymbol{\omega}\wedge\boldsymbol{r}$. Next, it is necessary to define two subdomains: the rotating subdomain Ω_r and the stationary subdomain Ω_s , which are illustrated in Fig. 1. Then, the factor f_{MRF} can be used to define each subdomain as:

$$f_{\text{MRF}} = f_{\text{MRF}}(\boldsymbol{s}) = \begin{cases} 1, \text{ if } \boldsymbol{s} \in \Omega_r \\ 0, \text{ if } \boldsymbol{s} \in \Omega_s \end{cases} , \tag{4}$$

where $\boldsymbol{s}$ is the coordinate of each point in the fluid domain.

The set of fluid flow equations that is valid for the whole domain, including the stationary and rotating subdomains, becomes:

$$\begin{aligned} &\nabla\bullet\boldsymbol{v}_{\text{abs}} = 0, \text{ and} \\ &\rho\nabla\boldsymbol{v}_{\text{abs}}\bullet\boldsymbol{v}_{\text{abs}} + f_{\text{MRF}}\left[-\rho\nabla\boldsymbol{v}_{\text{abs}}\bullet(\boldsymbol{\omega}\wedge\boldsymbol{r})\right. \\ &-\rho\nabla(\boldsymbol{\omega}\wedge\boldsymbol{r})\bullet(\boldsymbol{v}_{\text{abs}} - \boldsymbol{\omega}\wedge\boldsymbol{r}) \\ &\left.+\rho 2\boldsymbol{\omega}\wedge(\boldsymbol{v}_{\text{abs}} - \boldsymbol{\omega}\wedge\boldsymbol{r}) + \rho\boldsymbol{\omega}\wedge(\boldsymbol{\omega}\wedge\boldsymbol{r})\right] = \\ &\nabla\bullet\boldsymbol{T} + \rho\boldsymbol{f} + (1 - f_{\text{MRF}})\boldsymbol{f}_{r,s}(\alpha) + f_{\text{MRF}}\boldsymbol{f}_{r,r}(\alpha). \end{aligned} \tag{5}$$

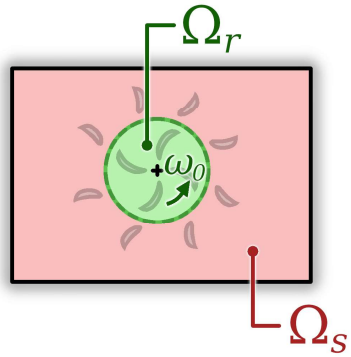

Figure 1: Illustration of the two subdomains for the MRF approach.

Note that, if eq. (5) is unfolded in polar/cylindrical coordinates, there will be a term that is based on the tangential derivative. This term is the basis of the MRF formulation, because it physically represents the *moving mesh*-like approximation. Note that, when assuming axisymmetry, this term becomes zero, meaning that the MRF formulation is essentially non-existent in the 2D swirl flow model.

2.1. Turbulence modeling

When applying a RANS model, a statistical time average is taken onto eq. (5), which leads to a set of equations with the same format, but with $\boldsymbol{T}$ being replaced by ($\boldsymbol{T} + \boldsymbol{T}_R$) (where $\boldsymbol{T}_R$ is the Reynolds (turbulent) stress tensor), and the state variables from eq. (5) become their statistical time averaged counterparts ($\overline{\boldsymbol{v}}_{\text{abs}}$, $\overline{p}$). For simplicity, the statistical time averaged counterparts are represented here with the same notation as before ($\boldsymbol{v}_{\text{abs}}$, p); however, notice that this notation is representing statistical time averaged variables when considering turbulent flow.

While eq. (2) is deduced by considering the reference frame change formula for vector variables, the turbulence equations feature scalar variables. Therefore, by considering the reference frame change formula for scalar variables, the convective terms become $\boldsymbol{v}_{\text{abs}}\bullet\nabla()$ (stationary reference frame) and $\boldsymbol{v}\bullet\nabla()$(rotating reference frame). Therefore, the WA2018 model [17, 18] for the MRF formulation becomes:

$$\boldsymbol{T}_R = \mu_{\text{T}}(\nabla\boldsymbol{v}_{\text{abs}} + \nabla{\boldsymbol{v}_{\text{abs}}}^T), \ \mu_{\text{T}} = \rho f_\mu R_{\text{T}}, \text{ and} \tag{6}$$

$$\begin{aligned} &\rho[(1 - f_{\text{MRF}})\boldsymbol{v}_{\text{abs}} + f_{\text{MRF}}(\boldsymbol{v}_{\text{abs}} - \boldsymbol{\omega}\wedge\boldsymbol{r})]\bullet\nabla R_{\text{T}} = \\ &\nabla\bullet[(\sigma_R\rho R_{\text{T}} + \mu)\nabla R_{\text{T}}] \\ &+ \rho C_1 R_{\text{T}} S + f_1 C_{1,k\text{-}\omega}\rho\frac{R_{\text{T}}}{S}\nabla R_{\text{T}}\bullet\nabla S \\ &- \rho(1 - f_1)\min\left[C_{2,k\text{-}\varepsilon}R_{\text{T}}^2\left(\frac{\nabla S\bullet\nabla S}{S^2}\right), \ C_m\nabla R_{\text{T}}\bullet\nabla R_{\text{T}}\right] \\ &- \lambda_{R_{\text{T}}}\kappa(\alpha)R_{\text{T}}, \end{aligned} \tag{7}$$

where R_T is the undamped turbulent viscosity, $\lambda_{R_{\text{T}}}$ is a penalization parameter that attenuates turbulence inside the modeled solid material, $\kappa(\alpha)$ is the inverse permeability (used in topology optimization), and the remaining terms

are, from [18],

$$\boldsymbol{S} = \frac{1}{2}(\nabla \boldsymbol{v} + \nabla \boldsymbol{v}^T),\ S = \sqrt{2\boldsymbol{S}\bullet\boldsymbol{S}},$$
$$\boldsymbol{W} = \frac{1}{2}(\nabla \boldsymbol{v} - \nabla \boldsymbol{v}^T),\ W = \sqrt{2\boldsymbol{W}\bullet\boldsymbol{W}},$$
$$f_\mu = \frac{\chi^3}{\chi^3 + c_w^3},\ \chi = \frac{R_\mathrm{T}}{\nu},\ c_w = 8.54,$$
$$\eta = S \max\left[1,\ \left|\frac{W}{S}\right|\right],\ C_m = 8.0,$$
$$\sigma_R = f_1(\sigma_{k\text{-}\omega} - \sigma_{k\text{-}\varepsilon}) + \sigma_{k\text{-}\varepsilon},\ \sigma_{k\text{-}\varepsilon} = 1.0,\ \sigma_{k\text{-}\omega} = 0.72,$$
$$f_1 = \tanh(arg_1^4),$$
$$arg_1 = \frac{\nu + R_\mathrm{T}}{2}\frac{\eta^2}{C_\mu\ k_T|_{\text{log-layer}}\ \omega_T|_{\text{log-layer}}}, \tag{8}$$
$$k_T|_{\text{log-layer}} = \frac{\nu_T S}{\sqrt{C_\mu}},\ \omega_T|_{\text{log-layer}} = \frac{S}{\sqrt{C_\mu}},\ C_\mu = 0.09,$$
$$C_1 = f_1(C_{1,k\text{-}\omega} - C_{1,k\text{-}\varepsilon}) + C_{1,k\text{-}\varepsilon},$$
$$C_{2,k\text{-}\omega} = \frac{C_{1,k\text{-}\omega}}{\kappa^2} + \sigma_{k\text{-}\omega},\ C_{2,k\text{-}\varepsilon} = \frac{C_{1,k\text{-}\varepsilon}}{\kappa^2} + \sigma_{k\text{-}\varepsilon},$$
$$C_{1,k\text{-}\omega} = 0.0829,\ C_{1,k\text{-}\varepsilon} = 0.1284,$$
$$\kappa = 0.41 \text{ (von Kármán constant)},$$
$$\nu = \frac{\mu}{\rho} \text{ (kinematic viscosity)}.$$

2.2. Boundary value problem

The boundaries of an impeller-diffuser configuration are illustrated in Fig. 2, from a circular section of the full device. The boundary value problem for the MRF formulation considering turbulent flow can then be stated as:

$$\begin{aligned}
&[\text{Eq. (5) for } (\boldsymbol{T} + \boldsymbol{T}_R)] && \text{in } \Omega \\
&[\text{Eq. (7)}] && \text{in } \Omega \\
&\boldsymbol{v}_\mathrm{abs} = \boldsymbol{v}_{in} \text{ and } R_\mathrm{T} = R_{\mathrm{T},in} && \text{on } \Gamma_\mathrm{in} \\
&\boldsymbol{v}_\mathrm{abs} = \boldsymbol{\omega}\wedge\boldsymbol{r} \text{ and } R_\mathrm{T} = 0 \text{ m}^2/\text{s} && \text{on } \Gamma_r \\
&\boldsymbol{v}_\mathrm{abs} = \boldsymbol{0} \text{ and } R_\mathrm{T} = 0 \text{ m}^2/\text{s} && \text{on } \Gamma_s \\
&(\boldsymbol{T} + \boldsymbol{T}_R)\bullet\boldsymbol{n} = \boldsymbol{0} \text{ and } \nabla R_\mathrm{T}\bullet\boldsymbol{n} = 0 && \text{on } \Gamma_\mathrm{out} \\
&[\text{Cyclic boundaries}] && \text{on } \Gamma_c,
\end{aligned} \tag{9}$$

where $\Omega = \Omega_r \cup \Omega_s$ is the full computational domain, Γ_in is the inlet boundary, Γ_out is the outlet boundary, Γ_r is the boundary of the rotating blades, Γ_s is the boundary of the stationary blades, and Γ_c indicates the cyclic boundaries. Cyclic boundaries are a specific type of periodic boundaries applied to circular sectors, in which the velocity vectors *enter* through one of the boundaries and *exit* through the other one, while keeping the same tangential and radial flow directions – i.e., the periodicity is set with respect to the tangential and radial directions. Since each quantity of blades in topology optimization may lead to different local minima, these boundaries help imposing a certain minimum number of blades in the optimized design, and avoid the situation where all blades may turn out different, which could also lead to issues such as instability.

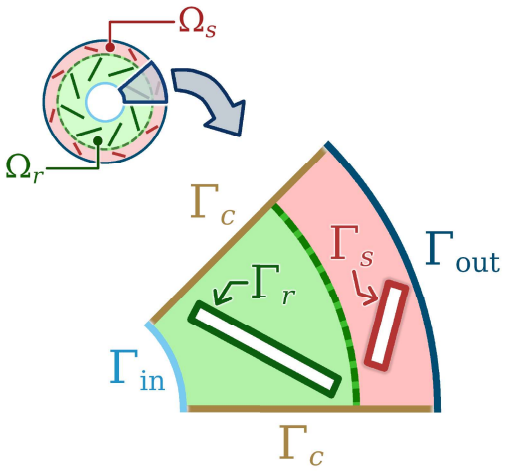

Figure 2: Illustration of the boundaries of an impeller-diffuser configuration.

3. Topology optimization problem formulation

The essential information for the topology optimization problem is defined as follows.

3.1. Material model for the MRF formulation

The solid and fluid parts of the design domain are defined from a continuous varying function [1]. The basic concept comes from the porous medium theory [39], where there is a resistance force of the porous medium that is proportional to the relative velocity through it. When this resistance force is sufficiently high, the porous medium acts as a solid, which means that it attains a solid body motion. Then, by considering rotating and stationary modeled solids:

$$\begin{aligned}
\boldsymbol{f}_r(\alpha) &= -\kappa_r(\alpha)\boldsymbol{v}_{\mathrm{mat},r}, \text{ and} \\
\boldsymbol{f}_s(\alpha) &= -\kappa_s(\alpha)\boldsymbol{v}_{\mathrm{mat},s},
\end{aligned} \tag{10}$$

where the relative velocities with respect to the modeled solids are given by $\boldsymbol{v}_{\mathrm{mat},r} = \boldsymbol{v}$ and $\boldsymbol{v}_{\mathrm{mat},s} = \boldsymbol{v}_\mathrm{abs}$. The inverse permeabilities for the rotating and stationary solids are given by $\kappa_r(\alpha)$ and $\kappa_s(\alpha)$, respectively. The variable α is commonly referred to as the *pseudo-density* and is the topology optimization design variable. Its values are used to denote solid ($\alpha = 0$) or fluid ($\alpha = 1$) materials, while the solid body motion is controlled by $\boldsymbol{v}_{\mathrm{mat},r}$ and $\boldsymbol{v}_{\mathrm{mat},s}$. Intermediary (*gray*) α values are permitted to relax the topology optimization formulation.

By converting the involved velocities to the same reference frame, assuming $\kappa_r(\alpha) = \kappa_s(\alpha) = \kappa(\alpha)$ (for simplicity), and defining a combined relative velocity with respect to the modeled solids as $\boldsymbol{v}_{\mathrm{mat},rs}$, the resistance force terms from eq. (5) may be changed as:

$$(1 - f_\mathrm{MRF})\boldsymbol{f}_{r,s}(\alpha) + f_\mathrm{MRF}\boldsymbol{f}_{r,r}(\alpha) = -\kappa(\alpha)\boldsymbol{v}_{\mathrm{mat},rs}, \tag{11}$$

where $\boldsymbol{v}_{\mathrm{mat},rs} = \begin{cases} \boldsymbol{v}_\mathrm{abs} - \boldsymbol{\omega}\wedge\boldsymbol{r}, & \text{if } \boldsymbol{s} \in \Omega_r \\ \boldsymbol{v}_\mathrm{abs}, & \text{if } \boldsymbol{s} \in \Omega_s \end{cases}$.

The change between solid and fluid is then controlled by the inverse permeability $\kappa(\alpha)$ as [1]:

$$\kappa(\alpha) = \kappa_{\max} + (\kappa_{\min} - \kappa_{\max})\alpha\frac{1+q}{\alpha+q}, \tag{12}$$

where $\kappa_{\max}$ is the maximum value, and $\kappa_{\min}$ is the minimum value. The penalization parameter $q > 0$ is used for the relaxation of the material model, where larger values mean less relaxation.

3.2. Topology optimization problem

The topology optimization problem can be defined as:

$$\begin{aligned}
&\textbf{min}_{\alpha}\ J(\boldsymbol{u}(\alpha), \alpha)\\
&\textbf{such that}\\
&\quad \text{Fluid volume constraints:}\\
&\quad \text{- Rotating zone:} \quad \int_{\Omega_{\alpha,r}} \alpha d\Omega_{\alpha,r} \leqslant\ f_r V_{r,0}\\
&\quad \text{- Stationary zone:} \quad \int_{\Omega_{\alpha,s}} \alpha d\Omega_{\alpha,s} \leqslant\ f_s V_{s,0}\\
&\text{Box constraint of } \alpha\text{: } 0 \ \leqslant\ \alpha \leqslant\ 1,
\end{aligned} \tag{13}$$

where $\boldsymbol{u}(\alpha) = \begin{bmatrix} p(\alpha) \\ \boldsymbol{v}_{\text{abs}}(\alpha) \\ R_T(\alpha) \end{bmatrix}$ is the state vector of the simulation for a given α; f_r and f_s are the specified maximum fluid volume fractions for the rotating and stationary zones, respectively (assumed, for simplicity, as $f_r = f_s = f$); $V_{r,0} = \int_{\Omega_{\alpha,r}} d\Omega_{\alpha,r}$ is the volume of the rotating zone of the design domain ($\Omega_{\alpha,r}$); $V_{s,0} = \int_{\Omega_{\alpha,s}} d\Omega_{\alpha,s}$ is the volume of the stationary zone of the design domain ($\Omega_{\alpha,s}$); and $J(\boldsymbol{u}(\alpha), \alpha)$ is the multi-objective function.

3.3. Multi-objective function

In order to optimize an impeller-diffuser configuration, four objectives are taken into account. The first objective is to minimize the *zone-relative energy dissipation*, which is based on [1] and Yoon [14] (turbulence effect), but also considers the inertial effects presented in Alonso et al. [40] only inside the rotating zone. This function is closely related to the pressure increment in Stokes flow [1], and to the pressure head in Navier-Stokes flow [41]. By assuming zero external body forces,

$$\begin{aligned}
\Phi_{\text{rel-z}} = \int_{\Omega} \Big[&\frac{1}{2}(\mu + \mu_{\text{T}})(\nabla \boldsymbol{v}_{\text{abs}} + \nabla \boldsymbol{v}_{\text{abs}}{}^{T})\bullet\\
&(\nabla \boldsymbol{v}_{\text{abs}} + \nabla \boldsymbol{v}_{\text{abs}}{}^{T})\Big] d\Omega\\
&- \int_{\Omega_r} \boldsymbol{f}_{r,r}(\alpha)\bullet(\boldsymbol{v}_{\text{abs}} - \boldsymbol{\omega} \wedge \boldsymbol{r}) d\Omega_r\\
&- \int_{\Omega_s} \boldsymbol{f}_{r,s}(\alpha)\bullet\boldsymbol{v}_{\text{abs}} d\Omega_s\\
&+ \int_{\Omega_r} (2\rho(\boldsymbol{\omega}\wedge(\boldsymbol{v}_{\text{abs}} - \boldsymbol{\omega} \wedge \boldsymbol{r})) + \rho\boldsymbol{\omega}\wedge(\boldsymbol{\omega}\wedge\boldsymbol{r}))\bullet\\
&(\boldsymbol{v}_{\text{abs}} - \boldsymbol{\omega} \wedge \boldsymbol{r}) d\Omega_r.
\end{aligned} \tag{14}$$

The second objective is to give more importance to the maximization of the performance of the rotor. More specifically, to increase the importance of the indirect relation of eq. (14) to the pressure head inside the rotor [41, 42]. In order not to depend on the definition of internal boundaries in the mesh, the equation is expressed as a cyclic integral (which requires using the relative velocity for the integrals), Gauss's divergence theorem is applied, and the *rotor relative pressure head* becomes:

$$\begin{aligned}
H_{\text{rel},r} = \frac{1}{Q}\int_{\Omega_r} \nabla\bullet \Big[&\left(\frac{p}{\rho g} + \frac{|\boldsymbol{v}_{\text{abs}} - \boldsymbol{\omega} \wedge \boldsymbol{r}|^2}{2g}\right)\\
&(\boldsymbol{v}_{\text{abs}} - \boldsymbol{\omega} \wedge \boldsymbol{r})\Big] d\Omega_r,
\end{aligned} \tag{15}$$

where g is the gravity acceleration (9.8 m/s^2), and Q is the flow rate.

The third objective is to increase the static pressure energy gained inside the diffuser. The static pressure energy is here given as a *variation of static pressure in the diffuser weighted by the flow rate*. In order not to depend on the definition of internal boundaries in the mesh, Gauss's divergence theorem is applied, leading to:

$$\Delta p_{Q,s} = \frac{1}{Q}\int_{\Omega_s} \nabla\bullet(p\boldsymbol{v}_{\text{abs}}) d\Omega_s. \tag{16}$$

Since the first and second objectives are relative measures (related to performance/dissipation), and the third objective is an absolute measure (related to an absolute quantity), it is possible for the third objective to pull the overall energy transfer down while still improving the performance – i.e., by reducing the overall energy transfer, it is possible that the variation of static pressure increases, while the energy dissipation drops. Therefore, the fourth objective is to increase the overall energy transferred from the whole device to the fluid. This is done through the *(absolute) pressure head*. By assuming zero external body

forces,

$$H = \frac{1}{Q}\left[\int_{\Gamma_{\text{in}}}\left(\frac{p}{\rho g}+\frac{|\boldsymbol{v}_{\text{abs}}|^2}{2g}\right)\boldsymbol{v}_{\text{abs}}\bullet\boldsymbol{n}d\Gamma + \int_{\Gamma_{\text{out}}}\left(\frac{p}{\rho g}+\frac{|\boldsymbol{v}_{\text{abs}}|^2}{2g}\right)\boldsymbol{v}_{\text{abs}}\bullet\boldsymbol{n}d\Gamma\right]. \tag{17}$$

These four objectives feature different measurement units (W/m, m, Pa and m, respectively), which have to be considered in the multi-objective function. By dividing each objective function by its corresponding value in the initial guess, considering the adequate sign for minimization (summation for maximization, subtraction for minimization), and then scaling by the initial value of one of the objective functions,

$$\begin{aligned} J = w_\Phi \Phi_{\text{z-rel}} &- w_{H,r}\left|\frac{\Phi_{\text{z-rel}}(\alpha_0)}{H_{\text{rel},r}(\alpha_0)}\right| H_{\text{rel},r} \\ &- w_{p,s}\left|\frac{\Phi_{\text{z-rel}}(\alpha_0)}{\Delta p_{Q,s}(\alpha_0)}\right| \Delta p_{Q,s} \\ &- w_{H,rs}\left|\frac{\Phi_{\text{z-rel}}(\alpha_0)}{H(\alpha_0)}\right| H, \end{aligned} \tag{18}$$

where α_0 is the distribution of the design variable in an initial configuration for the topology optimization, and w_Φ, $w_{H,r}$, $w_{p,s}$ and $w_{H,rs}$ are positive dimensionless weights ($w_\Phi, w_{H,r}, w_{p,s}, w_{H,rs} \geqslant 0$).

Although the four objective functions are interrelated directly or indirectly, in order to guarantee that one of them (or more) will be improved, it is necessary to explicitly set them in the multi-objective function. The format presented in eq. (18) may also be changed to a form that considers the dependency of the pressure head and the variation of pressure, with respect to the energy dissipation (see Appendix A).

4. Numerical implementation of the optimization

The numerical implementation of the topology optimization is illustrated in Fig. 3. The flowchart starts with setting the initial guess for the design variable α. The corresponding mesh is generated with the Gmsh software [43]. Then, the FEniCS software [34] is used to define the weak form of the problem, as well as the multi-objective function and the constraints, which are annotated by the dolfin-adjoint library [35]. This annotation procedure saves the structures of the weak form and integrations, enabling the later automatic derivation of the adjoint model. Then, the topology optimization algorithm (TOBS) is started [32, 33]. First, there is the TOBS linearization step, which requires the computation of the objective function, constraints and sensitivities. For the simulations, the OpenFOAM® [36] software is used. The OpenFOAM® software is an efficient CFD platform, and is more computationally efficient than FEniCS to model turbulent fluid flow [44], and also avoids the need to include possibly counter-intuitive modifications to the finite element model formulation with the sole aim of trying to achieve the convergence of the simulation [44] – such as intermediary projections, preconditioning part of the system of equations, derivative approximations, additional value limiters, pseudo-transient solution etc. The SIMPLE (Semi-Implicit Method for Pressure-Linked Equations) algorithm [45] is used for the simulations. However, OpenFOAM® does not provide an easy and efficient way to automatically derive the adjoint model, while FEniCS is able to do this automatic derivation efficiently through the dolfin-adjoint library. In order to make use of the advantages of both software platforms, the FEniCS TopOpt Foam library is used [37], being able to communicate the simulation from OpenFOAM® directly into the optimization framework of the dolfin-adjoint library. The conversion from the OpenFOAM® state variables to the FEniCS state variables consists of a discrete mapping and a projection including a small smoothing [46]. After receiving the necessary computed data from dolfin-adjoint, the linearized problem is solved by an integer programming optimizer (CPLEX® , from IBM). This is followed by the update of the design variable distribution α, and the verification of a specified tolerance. After meeting the specified tolerance, the topology optimization is finalized. A Helmholtz pseudo-density filter [47] is also considered in the topology optimization. A pseudocode of the implementation is provided in Appendix C.

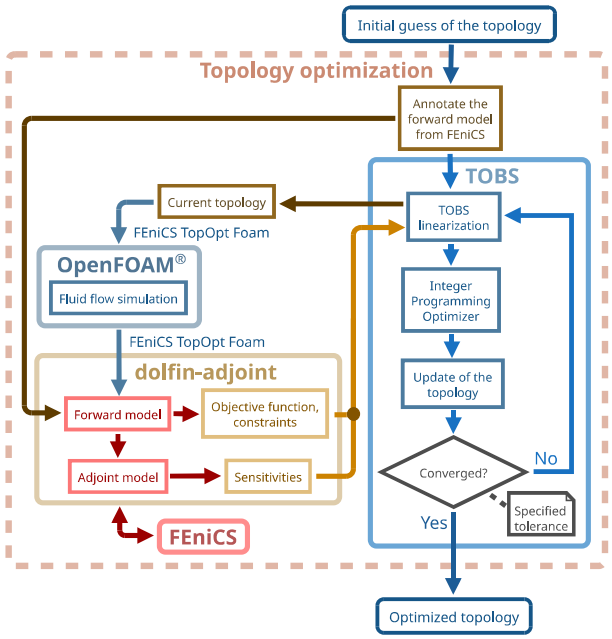

Figure 3: Flowchart of the numerical implementation of the topology optimization.

4.1. Finite element formulation

The implementation in FEniCS, which is used for the automatic derivation of the adjoint model, requires the definition of the finite element formulation. Note that the problem defined in Fig. 2 features cyclic boundaries, which

means that it would be more intuitive to view the periodic boundaries in polar coordinates (2D) or cylindrical coordinates (3D), rather than the usual Cartesian coordinates. This is shown in Fig. 4, where it can be seen that the cyclic boundaries become simple periodic boundaries when in polar/cylindrical coordinates, meaning that the degrees of freedom between both boundaries can be directly collapsed (i.e., merged). Thus, the finite element formulation is implemented in polar/cylindrical coordinates, and then mapped to Cartesian coordinates for visualization and for communicating with OpenFOAM® .

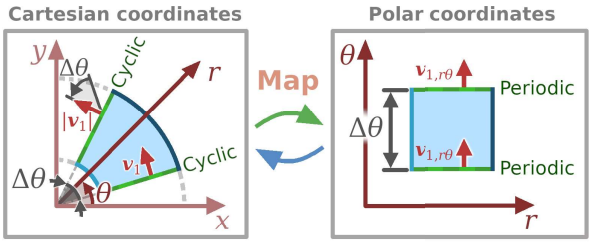

Figure 4: Cyclic boundaries.

In the finite element method, it is necessary to define the weak form of the problem for polar coordinates, which is shown in Appendix B. In order to couple the discretizations of pressure and velocity, the numerically stable MINI finite element formulation is used [48]. With respect to the traditional Taylor-Hood elements (quadratic velocity interpolation), MINI elements pose a lower computational cost (lower interpolation degree). Thus, the considered finite elements are: $P_1 + B_3$ for the velocity (nodal interpolation enriched by a cubic bubble function), P_1 for the pressure (nodal interpolation), P_1 for the undamped turbulent viscosity (nodal interpolation), and P_1 for the design variable (nodal interpolation).

4.2. TOBS formulation

The TOBS algorithm [32, 33] is a type of Sequential Integer Linear Programming (SILP), where sequentially linearized subproblems are solved while enforcing binary values for the design variable. The solution of each linearized subproblem is the *design variable step* $\Delta\alpha$. Since the TOBS algorithm is based on a linearization, there is a truncation error that arises from it and should be bounded through a constraint, resulting in an enforced small value [33]. Particularly, the truncation error constraint was originally presented in the discrete form assuming a perfectly uniform mesh in the topology optimization. In order to allow possible non-uniformities in the mesh, it is here extended to its integral form, by changing the original summation ($\|\Delta\alpha\|_1 = \sum_{i=0}^{n_\alpha}|\Delta\alpha_i| \leqslant \beta_{\text{flip limit}} n_\alpha$) to an integral and including the volume in the formulation in the place of the total number of the nodes ($\int_\Omega |\Delta\alpha| d\Omega \leqslant \beta_{\text{flip limit}} V_0$). Furthermore, it is split into the rotating and stationary subdomains, in order to take the presence of the two subdomains into account separately. Then, the *subdomain-aware* TOBS formulation for eq. (13) is given as:

$$
\begin{aligned}
&\min_{\Delta\alpha} \ \left.\frac{dJ}{d\alpha}\right|_{\alpha=\alpha_k} \Delta\alpha \\
&\textbf{such that} \\
&\quad \text{Inequality constraints:} \\
&\quad\quad \text{- Rotating zone:} \quad \left.\frac{dc_r}{d\alpha}\right|_{\alpha=\alpha_k} \Delta\alpha \leqslant \ \Delta c_r(\alpha_k) \\
&\quad\quad \text{- Stationary zone:} \quad \left.\frac{dc_s}{d\alpha}\right|_{\alpha=\alpha_k} \Delta\alpha \leqslant \ \Delta c_s(\alpha_k) \\
&\quad \text{Truncation error constraints:} \\
&\quad\quad \text{- Rotating zone:} \quad \int_{\Omega_r} |\Delta\alpha| d\Omega_r \leqslant \beta_{\text{flip limit}} V_{r,0} \\
&\quad\quad \text{- Stationary zone:} \quad \int_{\Omega_s} |\Delta\alpha| d\Omega_s \leqslant \beta_{\text{flip limit}} V_{s,0} \\
&\quad \text{Allowed values of } \Delta\alpha\text{: } \Delta\alpha \in \{\alpha_{lb} - \alpha_k, \alpha_{ub} - \alpha_k\},
\end{aligned}
\tag{19}
$$

where α_k is the design variable value in the beginning of the k optimization iteration; $\alpha_{lb} = 0$ and $\alpha_{ub} = 1$ are the lower and upper bounds, respectively; $c_r(\alpha) = \int_{\Omega_r} \alpha d\Omega_{\alpha,r}$; $c_s(\alpha) = \int_{\Omega_s} \alpha d\Omega_{\alpha,s}$; and $\beta_{\text{flip limit}}$ is a factor that limits the number of flips/jumps between 0 and 1. The design variable value for the next iteration is given as $\alpha_{k+1} = \alpha_k + \Delta\alpha$. When the bounds of the linearized inequality constraints ($\Delta c_r(\alpha_k)$ and $\Delta c_s(\alpha_k)$) are set as $f_r V_{r,0}$ and $f_s V_{s,0}$, the integer solution for eq. (19) may become unfeasible [33], depending on α_k. Thus, these bounds are relaxed as:

$$
\Delta c_i(\alpha_k) = \begin{cases} -\varepsilon_{\text{relax}}(c_i(\alpha_k) + c_{\text{ref},i}), \\ \quad \text{if } c_i(\alpha_k) > \frac{\varepsilon_{\text{relax}} c_{\text{ref},i}}{1-\varepsilon_{\text{relax}}} \\ -c_i(\alpha_k), \\ \quad \text{if } \frac{-\varepsilon_{\text{relax}} c_{\text{ref},i}}{1+\varepsilon_{\text{relax}}} \leqslant c_i(\alpha_k) \leqslant \frac{\varepsilon_{\text{relax}} c_{\text{ref},i}}{1-\varepsilon_{\text{relax}}} \\ \varepsilon_{\text{relax}}(c_i(\alpha_k) + c_{\text{ref},i}), \\ \quad \text{if } c_i(\alpha_k) < \frac{-\varepsilon_{\text{relax}} c_{\text{ref},i}}{1+\varepsilon_{\text{relax}}}, \end{cases}
\tag{20}
$$

where $i = r$ or s, $c_{\text{ref},r} = f_r V_{r,0}$, $c_{\text{ref},s} = f_s V_{s,0}$, and $0 < \varepsilon_{\text{relax}} < 1$ is a constraint relaxation parameter.

5. Numerical results

The numerical results are computed for water ($\mu = 0.001$ Pa s, $\rho = 1000.0$ kg/m^3), and the mesh is unstructured. Also, the presence of external body forces is neglected in the numerical examples ($\rho \boldsymbol{f} = (0,\ 0,\ 0)$), the specified fluid volume fraction (f) is selected as 70%, and $\kappa_{\min} = 0$ kg/(m^3 s). The TOBS algorithm is computed until $\Delta\alpha = 0$, or the topology has entered a slight loop

– i.e., when the topology is moving a little bit back and forth, but has, overall, already converged. The optimized topologies are plotted for the values of the pseudo-density (design variable) in the center of each finite element. The zones outside the design domain are removed from the system of equations being solved by TOBS.

The TOBS approach is carried out for $\varepsilon_{\text{relax}} = 0.05$ and $\beta_{\text{flip limit}} = 0.05$. In some cases, a continuation scheme in $\beta_{\text{flip limit}}$ is considered – for example, considering $\beta_{\text{flip limit}} = 0.05$ for some iterations, and then changing to $\beta_{\text{flip limit}} = 0.01$ or 0.005 in the next iterations. Similarly to continuation schemes in material model parameters, this continuation scheme is used in order to help reaching the optimized topology.

The initial guess for the pseudo-density (design variable) distribution consists of straight blades, which are indicated in Fig. 5. The indicated angles are set as $\beta_r = 30°$, $\beta_s = 15°$, and $\beta_{r\text{-}s} = 5°$, and the thickness of the rectangles is $e = 2$ mm, while the remaining dimensions are shown in Section 5.1. For the turbulent flow cases, the laminar flow topologies for similar configurations are considered as the initial guesses. Nonetheless, for a comparison standpoint, the variable α_0, from eq. (18), is still set according to the straight blades initial guess. In the rotor-only topology optimization results, only the set of blades of Fig. 5 that is inside the rotor zone is considered.

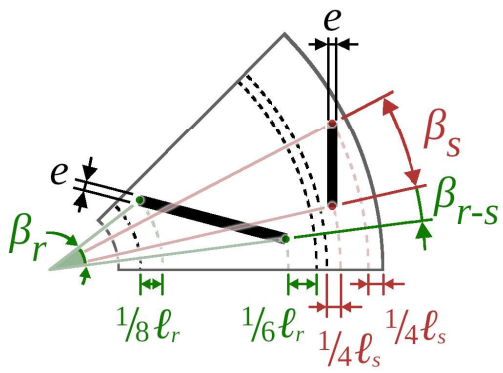

Figure 5: Straight blades initial guess, where the rotor straight blade is angularly centered.

The optimized topologies are the optimized distributions of the design variable, defining where there is solid and fluid. Therefore, it is possible to identify the contours of the fluid part of the domain. Since the topology optimization mesh is fixed, there will be some small roughness on the identified contours, whose effect was being atenuated during topology optimization, due to the use of the material model, the pseudo-density nodal design variable and the pseudo-density filter. Therefore, this small roughness should be smoothed (Fig. 6), either programatically or manually. All of the presented computed values, with the sole exception of convergence curves, are computed in the post-processed meshes, and are shown for the 45° section considered in the topology optimization – i.e., $1/8^{\text{th}}$ of the whole rotor.

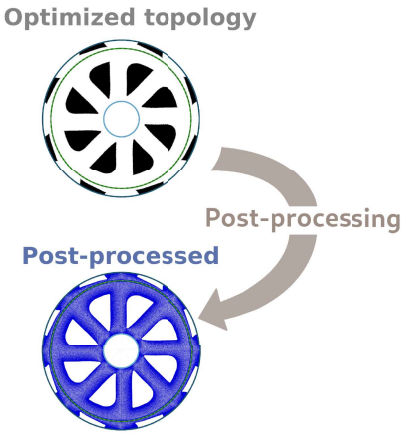

Figure 6: Post-processing of the optimized topologies, illustrated for the whole rotor.

The sensitivities are compensated by the volume around each design variable node, by considering a Riesz map in the sensitivity analysis, leading to mesh-independency in the computed sensitivities [49]. This is particularly interesting for non-uniform meshes, since non-uniformities lead to less-smooth sensitivities and may possibly hinder the topology optimization process. When there are periodic boundaries, this effect needs to take the mesh periodicity into account. This can be done by making use of the finite element variables from FEniCS, and computing the following equation:

$$\int_\Omega \left.\frac{dJ}{d\alpha}\right|_{L^2} w_{L^2} d\Omega = \frac{dJ}{d\alpha}, \tag{21}$$

where w_{L^2} is the test function for $\left.\frac{dJ}{d\alpha}\right|_{L^2}$. $\left.\frac{dJ}{d\alpha}\right|_{L^2}$ is the mesh-independent sensitivity, which mathematically corresponds to an L^2 inner product. In order to keep the same measurement units from the original equations, $\left.\frac{dJ}{d\alpha}\right|_{L^2}$ may then be multiplied by the average volume (sum of the volumes around each node, divided by the number of nodes). Under polar/cylindrical coordinates, the different coordinate system must also be considered in eq. (21) ($d\Omega = r d\Omega_c$).

The radius from the Helmholtz pseudo-density filter is set for slightly smoothing the contours of the optimized topology distributions, as half of the smallest element size in the mesh.

The Reynolds number is given as the maximum value of the local Reynolds number based on the external diameter:

$$\text{Re}_{\text{ext},\,\ell} = \frac{\mu\,|\boldsymbol{v}_{\text{abs}}|\,(2r_{ext})}{\rho}, \tag{22}$$

where r_{ext} is the external radius.

The inlet velocity profile, which is imposed on Γ_{in} (Fig. 2), is defined as a relative velocity in the radial direction.

The inlet turbulent variable ($R_{\mathrm{T},in}$) is given as:

$$R_{\mathrm{T},in} = \sqrt{\frac{n_v}{2}} I_T \ell_T |\boldsymbol{v}_{\mathrm{abs},in}|, \tag{23}$$

where I_T is the turbulence intensity (set as 5%), ℓ_T is the turbulence length scale, $|\boldsymbol{v}_{\mathrm{abs},in}|$ is the local absolute velocity on the inlet, and n_v is the number of velocity components (in 2D, 2 components). Also, ℓ_T is selected as $\ell_T = 0.07 C_\mu^{1/4} \ell_{\mathrm{in}}$ [50, 51] where ℓ_{in} is the length of the inlet contour for the whole rotor (i.e., $2\pi r_{int}$).

In the numerical results, the *variation of (static) pressure* Δp is computed as

$$\Delta p = \overline{p}_{out} - \overline{p}_{in} = \frac{\int_{\Gamma_{\mathrm{out}}} p d\Gamma_{\mathrm{out}}}{\int_{\Gamma_{\mathrm{out}}} d\Gamma_{\mathrm{out}}} - \frac{\int_{\Gamma_{\mathrm{in}}} p d\Gamma_{\mathrm{in}}}{\int_{\Gamma_{\mathrm{in}}} d\Gamma_{\mathrm{in}}}. \tag{24}$$

In order to accelerate the progress of the optimization, the OpenFOAM® simulations for each optimization step reuse the simulation result coming from the immediately previous optimization step. Since the resulting simulations are sequentially being converged, the maximum number of SIMPLE iterations per optimization step can also be reduced (e.g., depending on the case, 500∼2000 iterations per optimization step).

The numerical examples are presented in four parts. In the first part, some dimensions are varied in the rotor-diffuser design, and a single configuration for the dimensions is selected for the next numerical results. In the second part, the laminar flow design is compared to the turbulent flow design. In the third part, the rotor-diffuser design is shown for a rotor-only design. In the last part, the weights from the multi-objective function are varied, in order to show the importance of each of them.

5.1. Design domain and mesh

An impeller-diffuser configuration [24], also referred to as a *rotor-diffuser* configuration, is considered for topology optimization through a 2D model (*predominantly radial* impeller-diffuser – For other configurations, such as radial-axial configurations, a 3D model, which is more computationally costly would need to be considered). The impeller, which is also referred to as the *runner blades* or simply as the *rotor*, is the driving part of the device. The diffuser [52], also referred to as the *guide vanes* or the *diffuser ring*, can serve for two aims: the first one is to increase the static pressure energy of the outflow, and the second one is to adjust the direction of the outflow, in order to better match devices that are placed after the impeller-diffuser. Here, the topology optimization is set for the diffuser to help maximizing the total energy transferred to the fluid, and to maximize the variation of the static pressure in it, or, at least, to avoid dropping it too much in the optimized topologies.

The computational domain is shown Fig. 7, where the design domain is set only for the ℓ_r (rotor) and ℓ_s (diffuser) zones. The inlet length is set as ℓ_{in} (outside the design domain, set here as 5 mm), and the gap length is set as ℓ_g (outside the design domain), in order to avoid the rotating and stationary zones to touch each other. The basic radial dimensions are r_{ext} (external radius, for the outlet), and r_{int} (internal radius, for the inlet, set here as 15 mm). The MRF zone (rotating zone) is delimited by $\sqrt{x^2+y^2} < r_{\mathrm{MRF}}$, and r_{MRF} is given in the middle of the gap. The domain section is set for $\Delta\theta = 45°$, and the rotation is given according to the right-hand rule – i.e., in the z direction.

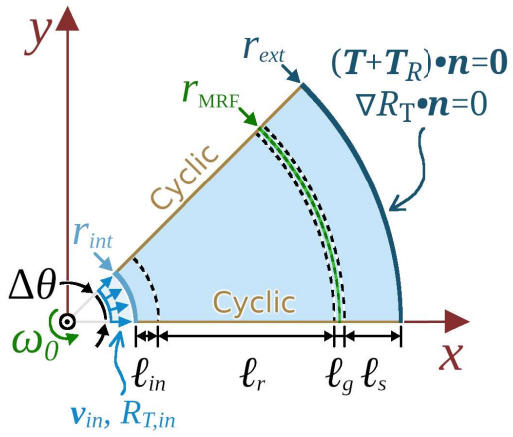

Figure 7: Computational domain.

The mesh being considered for the topology optimization is 2D and depends on the dimensions being considered. For $\ell_r = 38$ mm, $\ell_g = 2$ mm, and $\ell_s = 6$ mm, the mesh is shown in Fig. 8, with 57,510 elements.

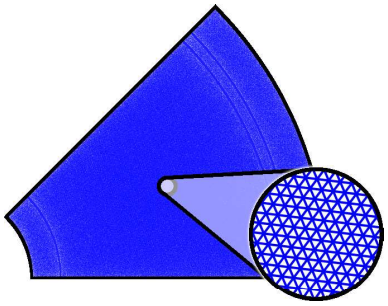

Figure 8: Mesh.

In the laminar flow examples, the radial inlet velocity is set as 0.001 m/s, and the rotation is set as 1.047×10^{-1} rad/s. For the turbulent flow case, the radial inlet velocity is set as 0.01 m/s, and the rotation is set as 1.047 rad/s.

5.2. Sizes of the gap and diffuser zones

The sizes of the gap (ℓ_g) and the diffuser (ℓ_s) zones are varied in the rotor-diffuser design, in order to show their effect in laminar flow topology optimization, before setting a single configuration for the dimensions in the next numerical results. The topology optimization results

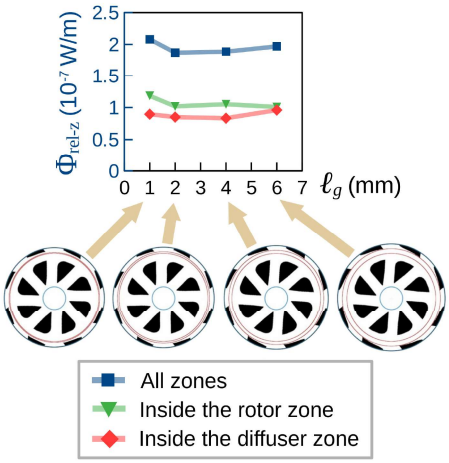

(a) *Zone-relative energy dissipation* $\Phi_{\text{rel-z}}$, separated into the rotor and diffuser zone integrations.

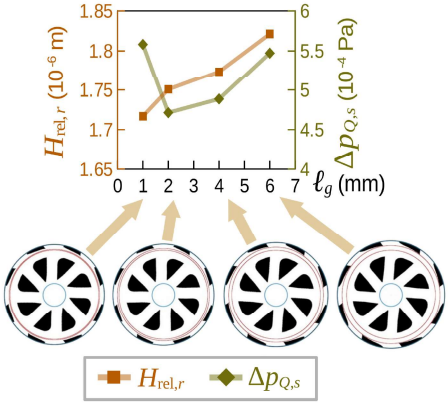

(b) *Rotor relative pressure head* $H_{\text{rel},r}$ and *variation of static pressure in the diffuser weighted by the flow rate* $\Delta p_{Q,s}$.

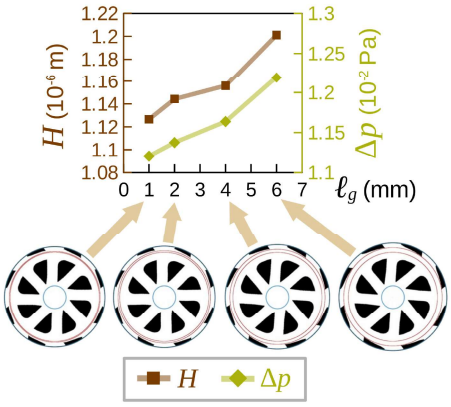

(c) *Pressure head* H and *variation of pressure* Δp.

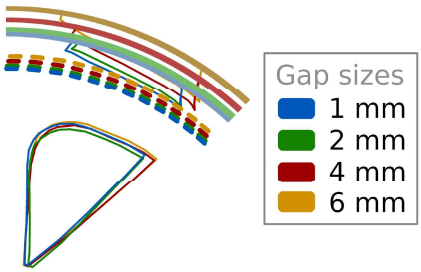

(d) Comparison of the optimized topologies for different gap sizes.

Figure 9: Topology optimization results for different gap sizes ($w_\Phi = 8$, $w_{H,r} = 1$, $w_{p,s} = 0.05$ and $w_{H,rs} = 5$).

for different gap sizes, by considering $\ell_r = 38$ mm and $\ell_s = 6$ mm, are shown in Fig. 9.

The optimized topologies are overlapped in Fig. 9d, and the dashed circumferences indicate the middle of the gaps. Note that larger gap sizes seem to make the flow path slightly more inclined. Furthermore, the diffuser zones are located in larger radii and feature larger blades as the gap size gets larger. The different gap sizes are indicated by the zone between the red circumferences in the optimized topologies from Figs. 9a to 9c. From Fig. 9a, the zone-relative energy dissipation $\Phi_{\text{rel-z}}$ considered in topology optimization seems to feature a minimum value near the gap size of 2 mm. This effect is also shown separated into the rotor and diffuser zones, which show different behaviors; the rotor zone effect seems to also have a minimum value near the 2 mm gap size – however, it diminishes for even larger gap sizes; and the diffuser zone seems to have a minimum value near the 4 mm gap size, increasing for even larger gap sizes. The increase in the energy dissipation of the diffuser can be viewed as a consequence of the diffuser being located at larger radii, which means that the diffuser zone is larger, and larger zones are more prone to dissipating energy. The rise in the rotor relative pressure head $H_{\text{rel},r}$ (Fig. 9b) shows that the overall performance of the rotor seems to improve for larger gaps. The variation of pressure in the diffuser zone $\Delta p_{Q,s}$ shows a similar behavior; however, there seems to be a minimum value at the 2 mm gap size, which can be caused by the different angulations of the flow around the rotor and diffuser blades. Finally, the pressure head H and the variation of pressure Δp show similar behaviors, increasing at larger gaps. Therefore, in the overall, larger gap sizes seem to help transferring energy to the fluid more efficiently, although this behavior may change at smaller gap sizes, most probably due to the smaller consequent diffuser size.

By considering a 2 mm gap size ($\ell_g = 2$ mm), and $\ell_r = 38$ mm, the topology optimization results for different diffuser sizes are given in Fig. 10.

From Fig. 10d, the effect of the larger size of the diffuser slightly affects the shape of the rotor blades, making them more inclined, while the diffuser becomes more prominent. The larger diffuser size caused a decrease in the zone-relative energy dissipation $\Phi_{\text{rel-z}}$ due to the effect in the rotor zone, although the diffuser zone tried increasing it (from its larger size) (Fig. 10a). In this case, a worse performance (rotor relative pressure head $H_{\text{rel},r}$) is observed for the rotor (Fig. 10b), as well as a larger static pressure rise inside the diffuser $\Delta p_{Q,s}$ (done mostly from the larger size) (Fig. 10b), and a rise in the pressure head H and the static pressure Δp (Fig. 10c). Therefore, larger diffuser zones seem to help transferring energy to the fluid, although at the cost of the performance of the rotor (rotor relative pressure head $H_{\text{rel},r}$).

From this section onwards, for evaluating other effects, the dimensions are set as $\ell_g = 2$ mm, $\ell_r = 38$ mm, and $\ell_s = 6$ mm.

5.3. Turbulent flow

The rotor-diffuser is optimized for turbulent and laminar flows, and the convergence curves of the topology optimization are shown in Fig. 11. The simulation results are shown in Fig. 12, where $\boldsymbol{v}_{\text{rel}}$ corresponds to all velocities viewed from the rotating reference frame. By comparing the optimized topologies in Fig. 12, the rotor blades in the turbulent case are more tilted back, while there are also splitter diffuser blades, which are not present in the laminar flow case. From the velocity plots from Fig. 12, the diffuser blades change the outflow direction, reducing its spinning component, which was highly increased by the rotation of the rotor and is, in fact, one of the objectives of this type of device. Also, the major pressure rise happens inside the rotor (Fig. 12), showing its pumping power. The plot of the turbulent viscosity (Fig. 12b) shows that the turbulence is more apparent going outside the inlet, which seems to be an effect of the inlet turbulence and the shape of the rotor blades, and rises again when reaching the diffuser blades, due to the change in the flow direction.

In order to gain a better insight on the optimized topologies, the simulations of the straight blades are shown in Fig. 13. Note that, in the turbulent flow case, the straight blades suffer from flow separation (recirculation zones) behind them, which increases energy dissipation. These recirculation zones are completely avoided in the optimized topologies, and the induced turbulence (μ_{T}) is much smaller (about 10 times smaller).

The computed values in the laminar and turbulent flow optimized topologies are shown in Table 1. The corresponding maximum local Reynolds numbers in the optimized topologies are 6.5×10^2 and 6.4×10^3, respectively. From Table 1, the laminar flow optimized topology is shown to dissipate less energy ($\Phi_{\text{rel-z}}$) than the straight blades initial guess, being caused mainly by the reduction in the dissipation of the diffuser zone $\Phi_{\text{rel-z}}|_{\text{s}}$. The static pressure rise Δp is also shown some improvement. The other values are slightly worse in the optimized topology; however, this is mostly due to the considered objective function weights, which prioritized the reduction of the energy dissipation (capable of giving a smoother flow inside the rotor that dissipates less energy). As an example, if the weight of the pressure head $w_{H,rs}$ (= 0.5) is increased to, for example, 10.0, the new optimized topology features a pressure head H that is 25% higher, although the other values are slighlty worsened. When performing this same comparison for the turbulent flow case, the turbulent flow optimized topology is shown to feature much less energy dissipation $\Phi_{\text{rel-z}}$, the rotor relative pressure head $H_{\text{rel},r}$ is shown a 16% improvement, the variation of pressure in the diffuser $\Delta p_{Q,s}$ and the pressure head H are worsened, and the variation of static pressure Δp is improved by 45%. The improvements under turbulent flow are shown to be different from laminar flow, and may possibly be attributed to: the optimized topology itself, which induces a smoother flow that reduces potential turbulence sources;

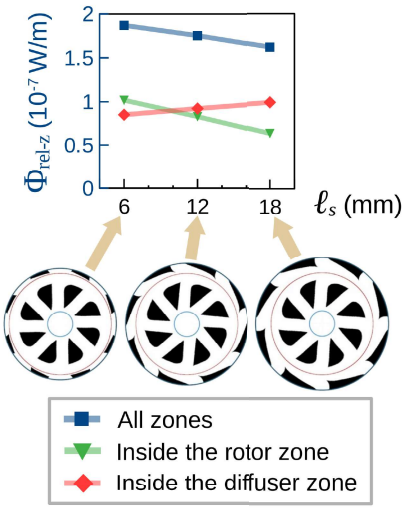

(a) *Zone-relative energy dissipation* $\Phi_{\text{rel-z}}$, separated into the rotor and diffuser zone integrations.

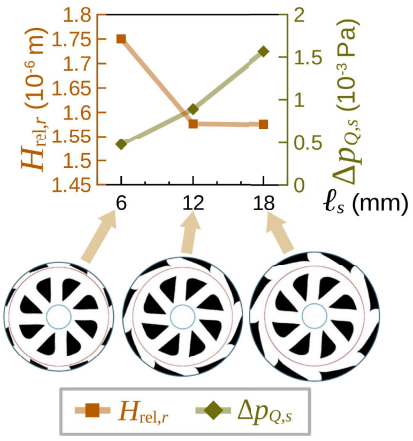

(b) *Rotor relative pressure head* $H_{\text{rel},r}$ and *variation of static pressure in the diffuser weighted by the flow rate* $\Delta p_{Q,s}$.

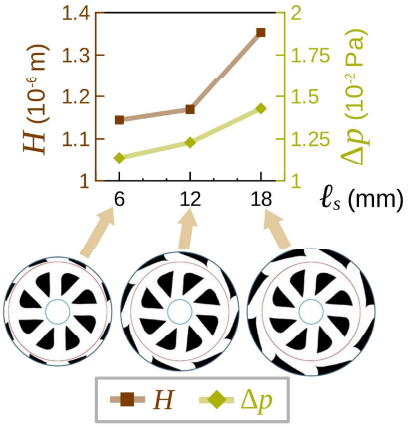

(c) *Pressure head* H and *variation of pressure* Δp.

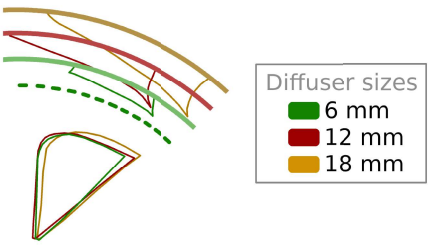

(d) Comparison of the optimized topologies for different diffuser sizes.

Figure 10: Topology optimization results for different diffuser sizes ($w_\Phi = 8$, $w_{H,r} = 1$, $w_{p,s} = 0.05$ and $w_{H,rs} = 5$).

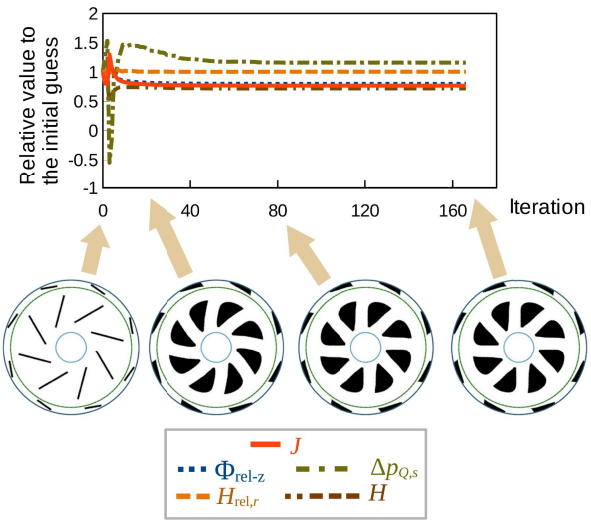

(a) For laminar flow.

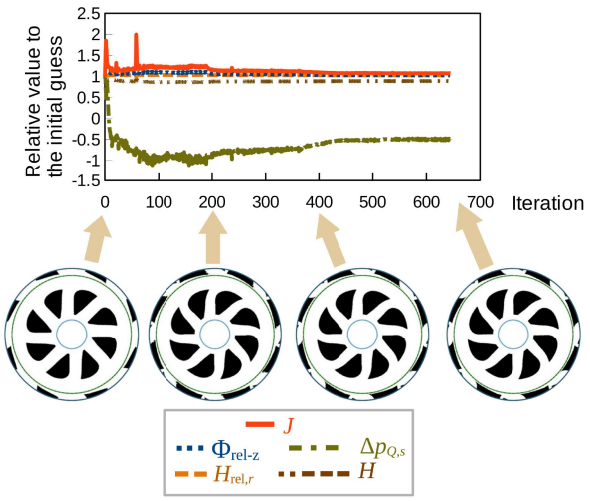

(b) For turbulent flow (Obs. $\beta_{\text{flip limit}} = 0.05$ is changed to 0.01 in the 192$^{\text{nd}}$ iteration, and to 0.005 in the 365$^{\text{th}}$ iteration).

Figure 11: Convergence curves ($w_\Phi = 8$, $w_{H,r} = 1$, $w_{p,s} = 0.05$ and $w_{H,rs} = 0.5$). The objective function values are given with respect to their values at the initial iteration.

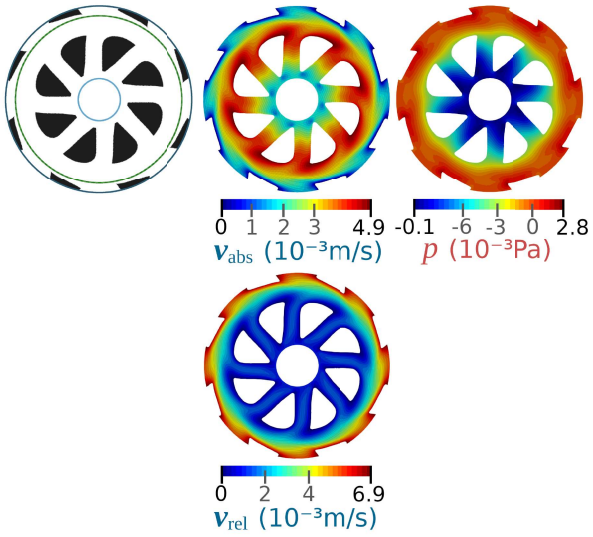

(a) Laminar flow.

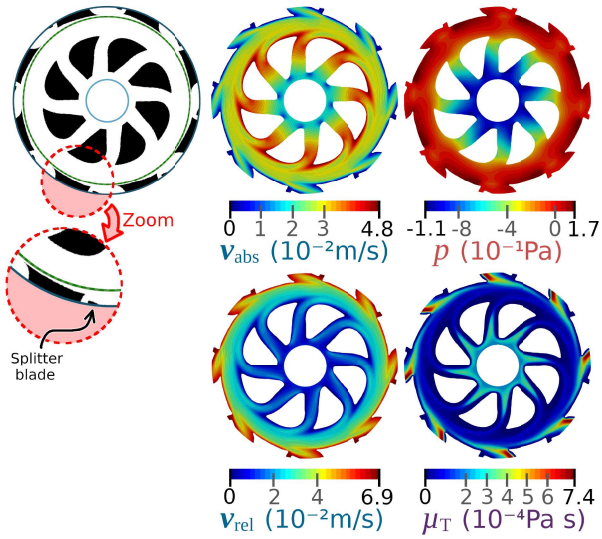

(b) Turbulent flow.

Figure 12: Simulations of the laminar and turbulent optimized topologies ($w_\Phi = 8$, $w_{H,r} = 1$, $w_{p,s} = 0.05$ and $w_{H,rs} = 0.5$).

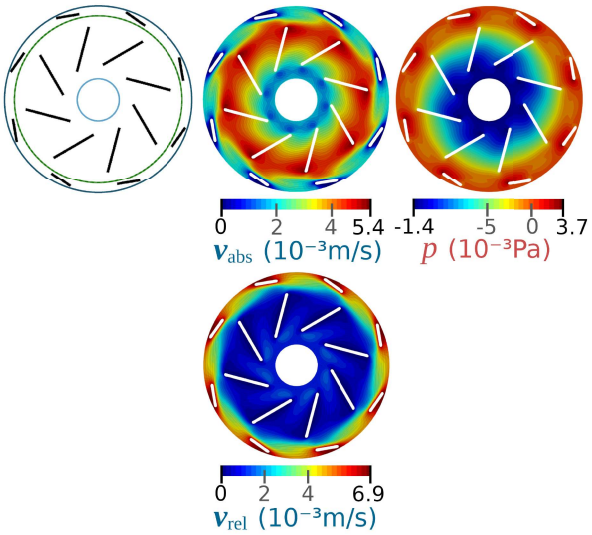

(a) Laminar flow.

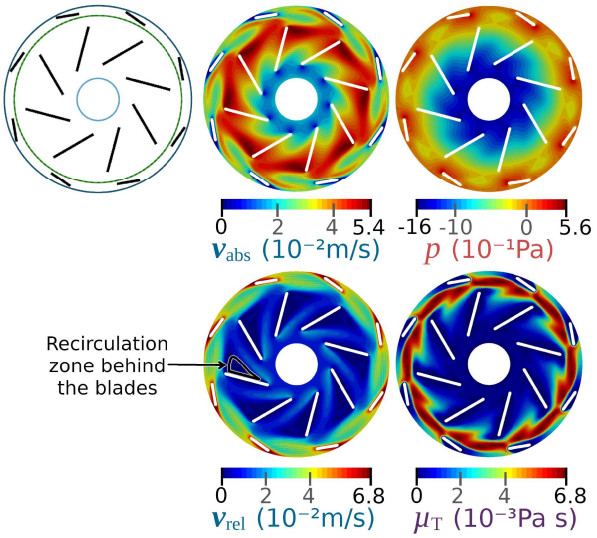

(b) Turbulent flow.

Figure 13: Simulations of the laminar and turbulent straight blades.

and also the different effects of the objective functions under turbulent flow, which may increase the importance of the some of the objective functions with respect to the energy dissipation.

Table 1: Computed values for the laminar and turbulent optimized (op.) topologies after post-processing, under laminar and turbulent flows, respectively. The values for the straight (st.) blades initial guess are also shown.

Case	$\Phi_{\text{rel-z}}$ (10^{-5}W/m)	$\Phi_{\text{rel-z}}\|_{\text{s}}$ (10^{-5}W/m)	$\Phi_{\text{rel-z}}\|_{\text{r}}$ (10^{-5}W/m)
Laminar (op.)	0.0165	0.0068	0.0097
Turbulent (op.)	4.9	2.3	2.6
Laminar (st.)	0.020	0.011	0.0090
Turbulent (st.)	11.49	6.85	4.64

$H_{\text{rel},r}$ (10^{-4}m)	$\Delta p_{Q,s}$ (10^{-2}Pa)	H (10^{-4}m)	Δp (10^{-1}Pa)
0.0171	0.027	0.0094	0.097
1.79	-2.2	1.0	9.7
0.0174	0.021	0.013	0.13
1.54	7.40	1.6	14.02

The laminar and turbulent topologies from Fig. 12 may be compared to one another (i.e., *cross-checked*), in order to show the effects of *extrapolating* the optimized topologies obtained from one type of fluid flow to another. This is shown in Table 2. For simplicity, from here onwards, the topology optimized under laminar flow is referred to as *laminar topology*, and the one optimized under turbulent flow is referred to as *turbulent topology*. From the laminar flow results in Table 2, when considering the turbulent topology, all of the shown functions worsened, with the sole exception of the energy dissipation in the diffuser zone $\Phi_{\text{rel-z}}|_{\text{s}}$, which slightly improved. In the case of turbulent flow, the lack of the splitter blade in the laminar topology, as well as the differently shaped rotor and diffuser blades, caused a decrease in the energy dissipation $\Phi_{\text{rel-z}}$, and slightly improved the rotor relative pressure head $H_{\text{rel},r}$. On the other hand, the variation of pressure in the diffuser $\Delta p_{Q,s}$, as well as the pressure head H and the variation of static pressure Δp, worsened. Therefore, in the overall, the behavior of the topologies under different flow conditions seems to be quite unpredictable in the sense that the computed values may become worse. In order to assess the improvement more predictably, it is better to consider the same flow configuration from the optimization, and the objective function weights can be varied, which will be shown in Section 5.5.

Table 2: Comparison of the optimized topologies when under laminar and turbulent flows*.

Case	$\Phi_{\text{rel-z}}$ (10^{-5}W/m)	$\Phi_{\text{rel-z}}\|_{\text{s}}$ (10^{-5}W/m)	$\Phi_{\text{rel-z}}\|_{\text{r}}$ (10^{-5}W/m)
Laminar (o.l.)	0.0165	0.0068	0.0097
Laminar (o.t.)	0.0206	0.0055	0.0151
Turbulent (o.t.)	4.9	2.3	2.6
Turbulent (o.l.)	5.4	2.3	3.1

$H_{\text{rel},r}$ (10^{-4}m)	$\Delta p_{Q,s}$ (10^{-2}Pa)	H (10^{-4}m)	Δp (10^{-1}Pa)
0.0171	0.027	0.0094	0.097
0.0165	-0.057	0.0051	0.060
1.79	-2.2	1.0	9.7
1.73	3.3	1.2	11.2

* Legend:
o.l. = optimized topology for laminar flow.
o.t. = optimized topology for turbulent flow.

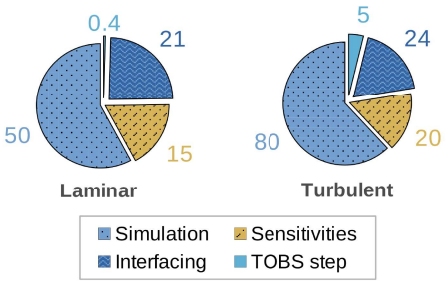

Figure 14: Average/typical timings for each optimization iteration (in seconds).

In order to get a brief insight on the computational cost of the performed topology optimization, the average/typical timings for each optimization iteration are shown in Fig. 14. Note that this number has to be multiplied by the number of the required iterations in order to give the total time of the topology optimization, which may be high. In Fig. 14, the computations were performed with only OpenFOAM® running in parallel (4 processes), for a maximum of 500 iterations for the simulation in each optimization step. The *interfacing* from Fig. 14 corresponds to converting to and from OpenFOAM® , whilst the *TOBS step* from Fig. 14 corresponds to solving eq. (19). Under laminar flow, the optimization iteration takes about 1 minute and a half, whilst under turbulent flow, the optimization iteration takes about 2 minutes. This is understandable from the sense that there are more state variables in the case of turbulent flow. Note that the *TOBS step* part consists of the smallest of the timings although it solves an integer optimization problem, which is normally expected to take longer, meaning that the implementation in CPLEX® is quite efficient. The main source of computational cost is the forward problem (simulation), which can still be improved by considering more processes when running the OpenFOAM® simulations, or using a smaller maximum number of iterations in OpenFOAM® for each optimization iteration (with some care so as not to deteriorate the ongoing topology optimization). The sensitivities' and interfacing timings can also still be improved by considering an iterative solver for the linear problems (such as GMRES), and/or parallelism in the adjoint model and in the projections.

5.4. Rotor-only configuration

Since previous works considered only the topology optimization of the rotor [9, 42, 53], the topology optimization of only the rotor is also performed here, in order to compare with the rotor-diffuser configuration. For this, the computational domain from Fig. 7 is considered up to the radius $r_{int}+\ell_{in}+\ell_r$, meaning that the topology optimization may be performed entirely inside the rotating reference frame, which simplifies the formulation. Note that, here, the rotation is given according to the right-hand rule (z direction), instead of the left-hand rule ($-z$ direction), which was considered in [9] and Sá et al. [53]. The optimized topologies, alongside their respective simulations, are shown in Fig. 15.

By comparing Fig. 15 with Fig. 12, note that the size of the rotor blades is larger, mainly due to neglecting the interaction with the diffuser, which dissipates energy and changes the outflow direction. Also, there are rotating blade splitters in Fig. 15, which may be attributed to the pressure head weight $w_{H,rs}$ (= 5.0) with respect to 0.5, which was considered in Fig. 12. The computed values are shown in Table 3. Note that the laminar flow topology is mostly better than the straight blades initial guess, with a slightly worse energy dissipation $\Phi_{\text{rel-z}}$. In the turbulent flow topology case, the optimized topology is notably better in terms of the pressure head H; however, it features worse values in the other values with respect to the straight blades initial guess. This is directly an effect of the weight of the pressure head $w_{H,rs}$ (= 5.0) and, if needed, $w_{H,rs}$ may be reduced in order for the other values to be able to improve, while worsening the pressure head H.

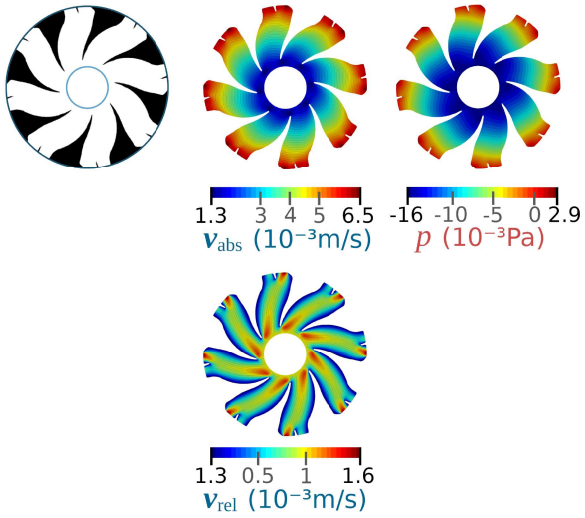

(a) Laminar flow.

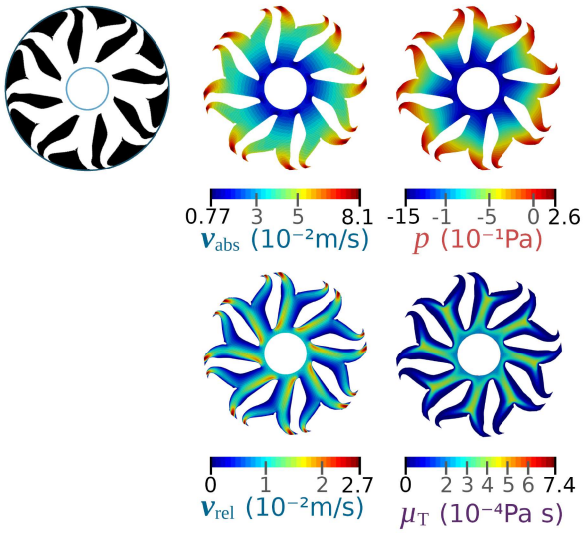

(b) Turbulent flow.

Figure 15: Simulations of the laminar and turbulent rotor-only optimized topologies ($w_\Phi = 8$, $w_{H,r} = 1$, and $w_{H,rs} = 5$).

Table 3: Computed values for the laminar and turbulent optimized (op.) rotor-only topologies after post-processing, under laminar and turbulent flows, respectively. The values for the rotor-only straight(st.) blades initial guess are also shown.

Case	$\Phi_{\text{rel-z}}$ (10^{-5}W/m)	$H_{\text{rel},r}$ (10^{-4}m)	H (10^{-4}m)	Δp (10^{-1}Pa)
Laminar (op.)	-0.0169	0.0154	0.033	0.149
Turbulent (op.)	-17.16	1.55	4.03	13.23
Laminar (st.)	-0.0170	0.0149	0.024	0.140
Turbulent (st.)	-18.037	1.57	2.15	13.92

In the overall, the rotor-only design neglects the presence of the diffuser, which allows it to better optimize the rotor. However, in some applications, it may be necessary to change the outflow characteristics through a diffuser, which affects the flow inside the rotor, and means that, in order to optimize it, the coupled phenomenon should be considered.

5.5. Weights of the multi-objective function

The weights of the multi-objective function are varied here, in order to show that each of the objective functions affects the overall design, creating a tendency to improve the corresponding value, which may or may not improve the other values.

The first weight to be varied is the one corresponding to the *zone-relative energy dissipation* (w_Φ). The results are shown in Fig. 16, for laminar and turbulent flows, where $f_{i,op}$ is the function i computed in the optimized topology, and $f_{i,st}$ is the function i computed in the straight blades configuration. On the images of the optimized topologies, when the main changes of each optimized topology with respect to the immediate left of it are possibly not easily noticeable, they are explicitly written on the images. For laminar flow (Fig. 16a), when increasing w_Φ, the rotor blades have a tendency of becoming shorter and narrower, which should make the fluid more smooth. Note that all of the other computed functions, with the exception of the ones related to the energy dissipation ($\Phi_{\text{rel-z}}$,$\Phi_{\text{rel-z}}|_{\text{s}}$, and $\Phi_{\text{rel-z}}|_{\text{r}}$), seem to get worse when increasing w_Φ. For turbulent flow (Fig. 16b), when increasing w_Φ, the optimized topology may arive at different solutions when trying to minimize the energy dissipation $\Phi_{\text{rel-z}}$, which can be seen on the two rightmost optimized topologies in Fig. 16b. One noticeable point is that the diffuser splitter blade has a tendency of becoming smaller under higher w_Φ, which may indicate that the diffuser splitter blade is not too favored by the energy dissipation $\Phi_{\text{rel-z}}$.

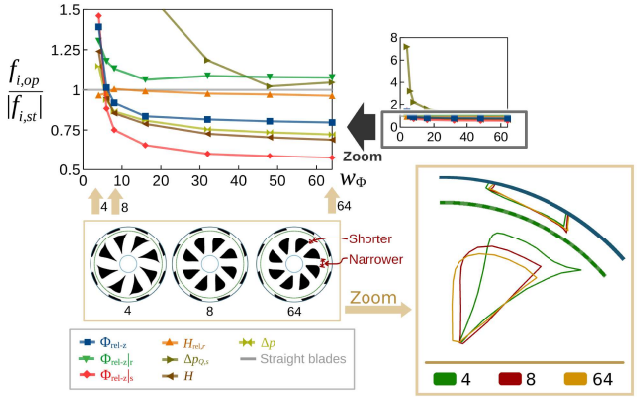

(a) For laminar flow ($w_{H,r} = 1$, $w_{p,s} = 0.05$, and $w_{H,rs} = 5$).

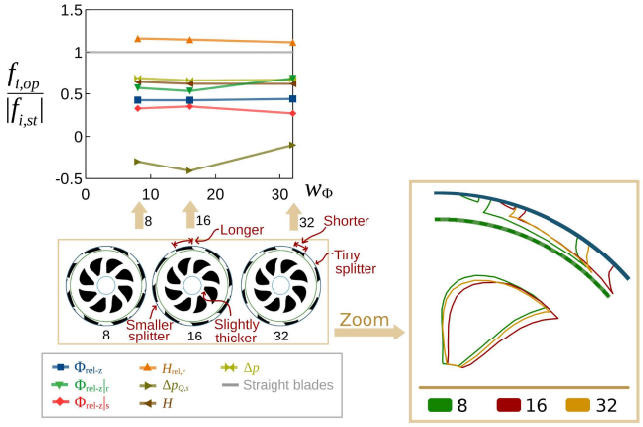

(b) For turbulent flow ($w_{H,r} = 1$, $w_{p,s} = 0.05$, and $w_{H,rs} = 0.5$).

Figure 16: Optimized topologies for different w_Φ values.

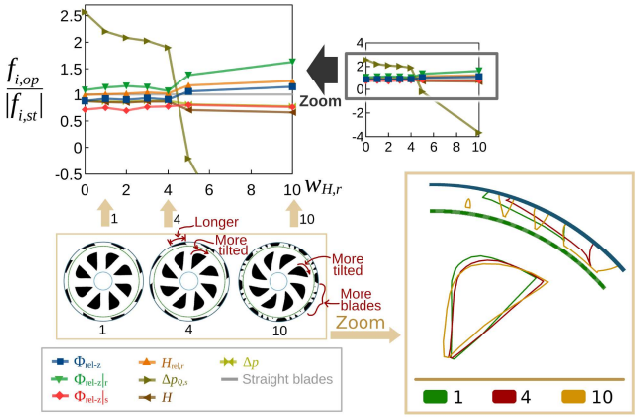

(a) For laminar flow ($w_\Phi = 8$, $w_{p,s} = 0.05$, and $w_{H,rs} = 5$).

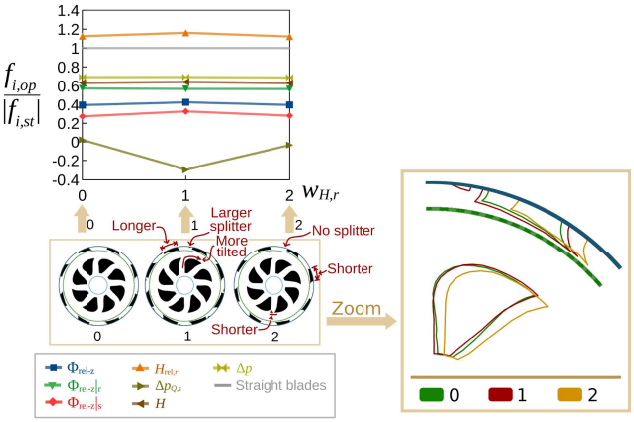

(b) For turbulent flow ($w_\Phi = 8$, $w_{p,s} = 0.05$, and $w_{H,rs} = 0.5$).

Figure 17: Optimized topologies for different $w_{H,r}$ values.

The second weight to be varied is the one corresponding to the *rotor relative pressure head* ($w_{H,r}$), shown in Fig. 17. For laminar flow (Fig. 17a), when increasing $w_{H,r}$, the rotor relative pressure head $H_{\text{rel},r}$ is also improved, especially when more diffuser blades appear in the optimized topology. However, the energy dissipation $\Phi_{\text{rel-z}}$ does not follow the same trend, and actually worsens (i.e., increases), as well as the other computed functions ($\Delta p_{Q,s}$, H, Δp). The additional diffuser blades seem to help decreasing the upward flow velocity near the exit of the rotating zone, which seems to help increasing the rotor relative pressure head $H_{\text{rel},r}$. For turbulent flow (Fig. 17a), when increasing $w_{H,r}$, the rotor blades seem to become more tilted towards the direction of the rotation, and shorter. The improvement in the rotor relative pressure head $H_{\text{rel},r}$ for the middle optimized topology is about 3.2% with respect to the leftmost optimized topology. The leftmost optimized topology featured a decrease of about 0.3% in the rotor relative pressure head $H_{\text{rel},r}$, which may indicate a local minimum.

The third weight to be varied is the one corresponding to the *variation of static pressure in the diffuser weighted by the flow rate* ($w_{p,s}$), shown in Fig. 18. For laminar flow (Fig. 18a), when increasing $w_{p,s}$, the optimized topology tends to have longer and straighter blades near the rotor exit. For $w_{p,s} \geqslant 0.4$, the optimized topology drastically changes, creating various auxiliary structures inside the rotor and changing the diffuser shape, aiming to increase the variation of pressure inside the diffuser $\Delta p_{Q,s}$. This comes, however, at the cost of the other function values, which get a tendency to worsen due to the now tortuous (less smooth) fluid flow path. For turbulent flow (Fig. 18b), when increasing $w_{p,s}$, the optimized topology tends to get shorter diffuser blades and rotor blades that are tilted more towards the direction of the rotation, as can be seen in the plots, while the only value that ends up getting slightly worse is the rotor relative pressure head $H_{\text{rel},r}$, which worsens about 1.75% with respect to the leftmost optimized topology, most probably due to the amount of blade tilting, which may not be the ideal one for improving it.

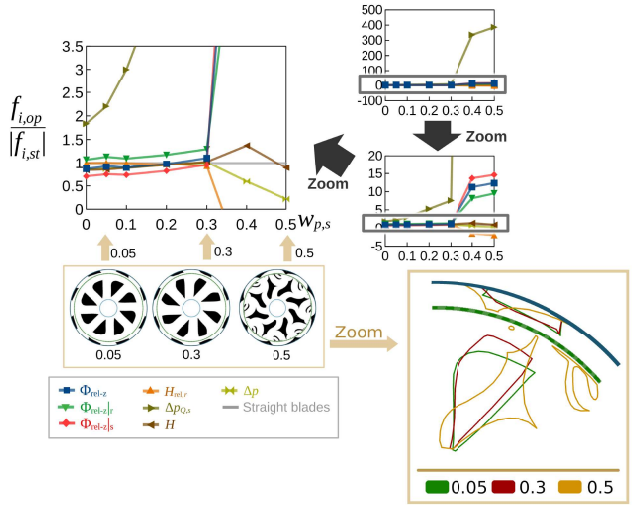

(a) For laminar flow ($w_\Phi = 8$, $w_{H,r} = 1$, and $w_{H,rs} = 5$).

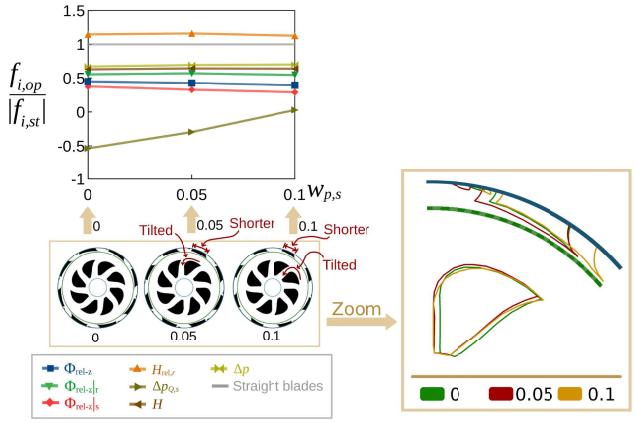

(b) For turbulent flow ($w_\Phi = 8$, $w_{H,r} = 1$, and $w_{H,rs} = 0.5$).

Figure 18: Optimized topologies for different $w_{p,s}$ values.

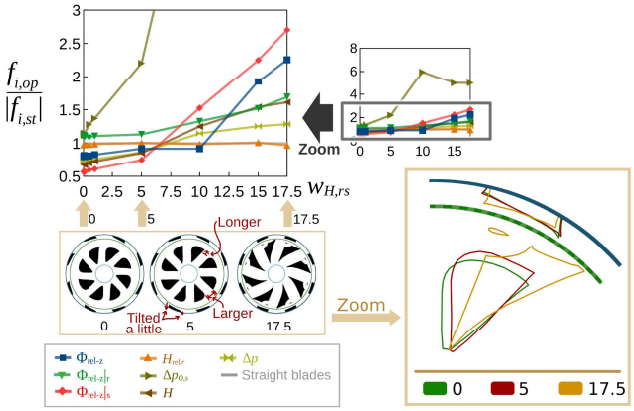

(a) For laminar flow ($w_\Phi = 8$, $w_{p,s} = 0.05$, and $w_{H,r} = 1$).

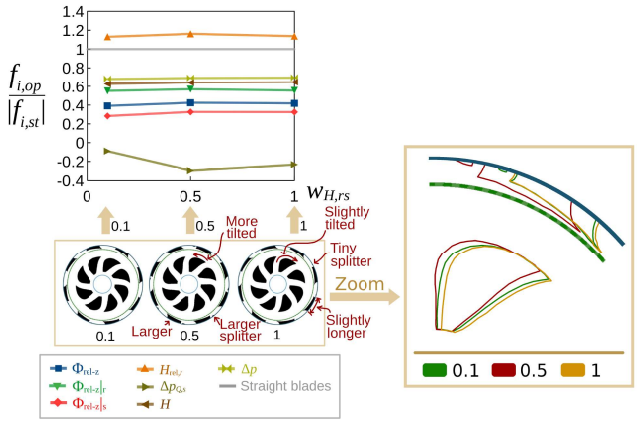

(b) For turbulent flow ($w_\Phi = 8$, $w_{p,s} = 0.05$, and $w_{H,r} = 1$).

Figure 19: Optimized topologies for different $w_{H,rs}$ values.

The fourth weight to be varied is the one corresponding to the *(absolute) pressure head* ($w_{H,rs}$), shown in Fig. 19. For laminar flow (Fig. 18a), when increasing $w_{H,rs}$, the rotor blades seem to favor longer sizes, which should be capable of delivering more power from the blades to the fluid. Overall, the functions related to the energy dissipation ($\Phi_{\text{rel-z}}$,$\Phi_{\text{rel-z}|\text{s}}$, and $\Phi_{\text{rel-z}|\text{r}}$) worsened, and the rotor relative pressure head $H_{\text{rel},r}$ slightly worsened. This can be seen from the fact that longer rotor blades are closer to the diffuser blades and, therefore, the interaction between blades is more intense (i.e., increases energy dissipation). For turbulent flow (Fig. 18b), when increasing $w_{H,rs}$, the optimized topologies seem to have reached different local minima in the topology optimization, where one of them features larger diffuser splitter blades and the other one tries to compensate the lack of diffuser splitter blades by changing the shapes of the rotor and diffuser blades. The improvement in the pressure head H for the two rightmost optimized topologies (from left to right) is 2.6% and 3.4%, with respect to the leftmost optimized topology.

6. Conclusions

In this work, the topology optimization method has been formulated for the MRF approach. The MRF approach consists of simulating the fluid flow inside the rotor zone according to the rotating reference frame, and inside the diffuser zone according to the stationary reference frame, in the form of a unified formulation. Also, a new combination for the multi-objective function is proposed for this case.

The numerical examples are presented for a 2D configuration, which means that the modeled impeller-diffuser is being simplified from a predominantly radial configuration. This simplification can be viewed as a design methodology, since it aims to make the analysis feasible in a topology optimization standpoint. Note that most works in pump optimization in literature consider parametric optimization, in which a small fixed set of parameters is considered, such as 10 parameters or some more, and the optimization ends up being quite restricted – i.e., it is unable to create splitters and change shapes. However, topology optimization operates by computing the sensitivities on each pixel/voxel of the design domain in order to define where to include or remove solid material, meaning

that there are millions of design variables (one for each pixel/voxel in the design domain), which significantly increases the computational cost, meaning that, in 3D realistic (well refined) models, it would necessarily require the use of High Performance Computing (HPC), which is not the focus of this paper. Nonetheless, in terms of a design methodology, it is normally good to have an initial insight on the optimization problem, and the use of a 2D model can possibly give at least a practical insight on the optimized configurations, since at least turbulence is being considered with a relatively realistic rotation. Thus, the use of a 2D model can be viewed as a first step in the overall design. It is not able to guarantee a 3D optimized result; however, it is systematic and may give a good insight on the problem. For example, the straight blades configuration was compared to the optimized topologies.

Four numerical examples are shown for: varying some dimensions in the rotor-diffuser design, comparing laminar and turbulent flow optimized topologies, showing the corresponding rotor-only design, and varying the weights in the multi-objective function. The dimensions of the rotor-diffuser design can affect the optimized topologies, albeit being fixed depending on the application. The turbulent flow is shown to affect the optimized topology, with respect to laminar flow. The rotor-only design neglects the presence of the diffuser ring, ignoring downstream effects, and may not be the best alternative depending on the application, when it is necessary to change the outflow characteristics through diffuser blades. The different importance of each objective function for the given application is represented by the multi-objective function weights, which lead to different optimized topologies.

As future work, some suggestions are to consider non-Newtonian fluids, thermal effects, the mixing plane approach, and other flow machine designs.

Acknowledgements

This research was partly supported by CNPq (Brazilian National Research Council) and FAPESP (São Paulo Research Foundation). The authors thank the supporting institutions. The first author thanks the financial support of FAPESP under grant 2022/07937-7. The second author thanks the financial support of CNPq (National Council for Research and Development) under grant 302658/2018-1 and of FAPESP under grant 2013/24434-0. The authors also gratefully acknowledge support of the RCGI – Research Centre for Greenhouse Gas Innovation, hosted by the University of São Paulo (USP) and sponsored by FAPESP – São Paulo Research Foundation (2014/50279-4 and 2020/15230-5) and Shell Brasil, and the strategic importance of the support given by ANP (Brazil's National Oil, Natural Gas and Biofuels Agency) through the R&D levy regulation.

Declarations of interest

None.

References

[1] T. Borrvall and J. Petersson, Topology optimization of fluids in Stokes flow, International Journal for Numerical Methods in Fluids 41 (2003) 77–107. URL: http://dx.doi.org/10.1002/fld.426. doi:10.1002/fld.426.

[2] A. Gersborg-Hansen, O. Sigmund and R. B. Haber, Topology optimization of channel flow problems, Structural and multidisciplinary optimization 30 (2005) 181–192.

[3] G. Pingen and K. Maute, Optimal design for non-Newtonian flows using a topology optimization approach, Computers & Mathematics with Applications 59 (2010) 2340–2350.

[4] E. Papoutsis-Kiachagias et al, Constrained topology optimization for laminar and turbulent flows, including heat transfer, CIRA, editor, EUROGEN, Evolutionary and Deterministic Methods for Design, Optimization and Control, Capua, Italy (2011).

[5] K. Yaji et al, Topology optimization in thermal-fluid flow using the lattice Boltzmann method, Journal of Computational Physics 307 (2016) 355–377. URL: http://www.sciencedirect.com/science/article/pii/S0021999115008244. doi:https://doi.org/10.1016/j.jcp.2015.12.008.

[6] L. F. N. Sá, C. M. Okubo Jr and E. C. N. Silva, Topology Optimization of Subsonic Compressible Flows, Structural and Multidisciplinary Optimization (2021). doi:https://doi.org/10.1007/s00158-021-02903-5.

[7] C. S. Andreasen, A. R. Gersborg and O. Sigmund, Topology optimization of microfluidic mixers, International Journal for Numerical Methods in Fluids 61 (2009) 498–513. URL: http://dx.doi.org/10.1002/fld.1964.

[8] K. E. Jensen, P. Szabo and F. Okkels, Topology optimizatin of viscoelastic rectifiers, Applied Physics Letters 100 (2012) 234102.

[9] J. Romero and E. Silva, A topology optimization approach applied to laminar flow machine rotor design, Computer Methods in Applied Mechanics and Engineering 279 (2014) 268 – 300. URL: http://www.sciencedirect.com/science/article/pii/S0045782514002151. doi:https://doi.org/10.1016/j.cma.2014.06.029.

[10] B. Zhang and X. Liu, Topology Optimization Study of Arterial Bypass Configurations Using the Level Set Method, Struct. Multidiscip. Optim. 51 (2015) 773–798. URL: http://dx.doi.org/10.1007/s00158-014-1175-y. doi:10.1007/s00158-014-1175-y.

[11] S. Lin et al, Topology optimization of fixed-geometry fluid diodes, Journal of Mechanical Design 137 (2015) 081402:1–081402:8.

[12] X. Duan, F. Li and X. Qin, Topology optimization of incompressible Navier–Stokes problem by level set based adaptive mesh method, Computers & Mathematics with Applications 72 (2016) 1131 – 1141. URL: http://www.sciencedirect.com/science/article/pii/S0898122116303662. doi:https://doi.org/10.1016/j.camwa.2016.06.034.

[13] L. F. N. Sá et al, Topological derivatives applied to fluid flow channel design optimization problems, Structural and Multidisciplinary Optimization 54 (2016) 249–264. URL: https://doi.org/10.1007/s00158-016-1399-0. doi:10.1007/s00158-016-1399-0.

[14] G. H. Yoon, Topology optimization for turbulent flow with Spalart–Allmaras model, Computer Methods in Applied Mechanics and Engineering 303 (2016) 288 – 311. URL: http://www.sciencedirect.com/science/article/pii/S004578251630007X. doi:https://doi.org/10.1016/j.cma.2016.01.014.

[15] C. B. Dilgen et al, Topology optimization of turbulent flows, Computer Methods in Applied Mechanics and Engineering 331 (2018) 363–393. doi:10.1016/j.cma.2017.11.029.

[16] G. H. Yoon, Topology optimization method with finite elements based on the k-ε turbulence model, Computer Methods in Applied Mechanics and Engineering 361 (2020) 112784. URL: http://www.sciencedirect.com/science/article/pii/S0045782519306760. doi:https://doi.org/10.1016/j.cma.2019.112784.

[17] D. H. Alonso et al, Topology optimization method based on the Wray-Agarwal turbulence model, Structural and Multidisciplinary Optimization 65 (2022) 1–24. doi:https://doi.org/10.1007/s00158-021-03106-8.

[18] X. Han, M. Rahman and R. K. Agarwal, Development and Application of Wall-Distance-Free Wray-Agarwal Turbulence Model (WA2018), in: 2018 AIAA Aerospace Sciences Meeting, 2018, p. 0593.

[19] T. J. Wray and R. K. Agarwal, Low-Reynolds-Number One-Equation Turbulence Model Based on k-ω Closure, AIAA Journal 53 (2015) 2216–2227.

[20] E. Moscatelli et al, Topology optimisation for rotor-stator fluid flow devices, Structural and Multidisciplinary Optimization 65 (2022) 1–23.

[21] B. C. de Souza, Topology optimization of fluid diodes based on integer linear programming., Ph.D. thesis, Universidade de São Paulo, 2021. URL: https://www.teses.usp.br/teses/disponiveis/3/3152/tde-18052021-134145/en.php.

[22] L. Sá et al, Continuous boundary condition propagation model for topology optimization, Structural and Multidisciplinary Optimization 65 (2022). doi:10.1007/s00158-021-03148-y.

[23] S. Huang et al, Numerical simulation of unsteady flow in a multistage centrifugal pump using sliding mesh technique, Progress in Computational Fluid Dynamics, An International Journal 10 (2010) 239–245.

[24] R. Elder, A. Tourlidakis and M. Yates, Advances of CFD in fluid machinery design, John Wiley & Sons, 2003.

[25] O. Petit and H. Nilsson, Numerical investigations of unsteady flow in a centrifugal pump with a vaned diffuser, International Journal of Rotating Machinery 2013 (2013).

[26] P. Adami et al, Multistage Centrifugal Pumps: Assessment of a Mixing Plane Method for CFD Analysis, in: 60 Congresso Nazionale ATI, 2005.

[27] L. F. N. Sá, Topology optimization method applied to ventricular assist device impeller and volute design., Ph.D. thesis, Universidade de São Paulo, 2019. URL: http://www.teses.usp.br/teses/disponiveis/3/3152/tde-16032017-103709/en.php.

[28] M. Zadravec, S. Basic and M. Hribersek, The influence of rotating domain size in a rotating frame of reference approach for simulation of rotating impeller in a mixing vessel, Journal of Engineering Science and Technology 2 (2007) 126–138.

[29] R. Franzke et al, Evaluation of the multiple reference frame approach for the modelling of an axial cooling fan, Energies 12 (2019) 2934.

[30] M. Benturki, R. Dizene and A. Ghenaiet, Multi-objective optimization of two-stage centrifugal pump using NSGA-II algorithm, Journal of Applied Fluid Mechanics 11 (2018) 929–943.

[31] L. Zhu, X. Zhang and Z. Yao, Shape optimization of the diffuser blade of an axial blood pump by computational fluid dynamics, Artificial organs 34 (2010) 185–192.

[32] B. C. Souza et al, Topology optimization of fluid flow by using Integer Linear Programming, Structural and Multidisciplinary Optimization (2021).

[33] R. Sivapuram and R. Picelli, Topology optimization of binary structures using Integer Linear Programming, Finite Elements in Analysis and Design 139 (2018) 49–61. URL: http://www.sciencedirect.com/science/article/pii/S0168874X17305619. doi:https://doi.org/10.1016/j.finel.2017.10.006.

[34] A. Logg, K.-A. Mardal and G. Wells, Automated solution of differential equations by the finite element method: The FEniCS book, volume 84, Springer Science & Business Media, 2012. URL: https://fenicsproject.org/book/.

[35] S. Mitusch, S. Funke and J. Dokken, dolfin-adjoint 2018.1: automated adjoints for FEniCS and Firedrake, Journal of Open Source Software 4 (2019) 1292. URL: https://doi.org/10.21105/joss.01292.

[36] H. G. Weller et al, A tensorial approach to computational continuum mechanics using object-oriented techniques, Computers in physics 12 (1998) 620–631.

[37] D. H. Alonso, L. F. Garcia Rodriguez and E. C. N. Silva, Flexible framework for fluid topology optimization with OpenFOAM® and finite element-based high-level discrete adjoint method (FEniCS/dolfin-adjoint), Structural and Multidisciplinary Optimization (2021). URL: https://link.springer.com/article/10.1007/s00158-021-03061-4. doi:https://doi.org/10.1007/s00158-021-03061-4.

[38] T. A. Davis, Algorithm 832: UMFPACK V4.3—an Unsymmetric-Pattern Multifrontal Method, ACM Trans. Math. Softw. 30 (2004) 196–199. URL: https://doi.org/10.1145/992200.992206. doi:10.1145/992200.992206.

[39] K. Vafai, Handbook of porous media, 2 ed., Crc Press, 2005.

[40] D. H. Alonso et al, Topology optimization based on a two-dimensional swirl flow model of Tesla-type pump devices, Computers & Mathematics with Applications 77 (2019) 2499 – 2533. URL: http://www.sciencedirect.com/science/article/pii/S0898122118307338. doi:https://doi.org/10.1016/j.camwa.2018.12.035.

[41] D. H. Alonso and E. C. N. Silva, Topology optimization applied to the design of Tesla-type turbine devices, Applied Mathematical Modelling 103 (2022) 764–791. URL: https://www.sciencedirect.com/science/article/pii/S0307904X21005370. doi:https://doi.org/10.1016/j.apm.2021.11.007.

[42] C. M. Okubo et al, Topology optimization applied to 3D rotor flow path design based on the continuous adjoint approach, Computers & Mathematics with Applications 96 (2021) 16–30. URL: https://www.sciencedirect.com/science/article/pii/S0898122121001863. doi:https://doi.org/10.1016/j.camwa.2021.05.006.

[43] C. Geuzaine and J.-F. Remacle, Gmsh: A 3-D finite element mesh generator with built-in pre- and post-processing facilities, International Journal for Numerical Methods in Engineering 79 (2009) 1309–1331. URL: https://onlinelibrary.wiley.com/doi/abs/10.1002/nme.2579. doi:https://doi.org/10.1002/nme.2579. arXiv:https://onlinelibrary.wiley.com/doi/pdf/10.1002/nme.2579.

[44] M. Mortensen, H. P. Langtangen and G. N. Wells, A FEniCS-based programming framework for modeling turbulent flow by the Reynolds-averaged Navier-Stokes equations, Advances in Water Resources 34 (2011) 1082–1101. URL: http://www.sciencedirect.com/science/article/pii/S030917081100039X. doi:https://doi.org/10.1016/j.advwatres.2011.02.013, new Computational Methods and Software Tools.

[45] S. V. Patankar, Numerical heat transfer and fluid flow, 1 ed., McGraw-Hill, 1980.

[46] D. H. Alonso and E. C. N. Silva, Topology optimization for blood flow considering a hemolysis model, Structural and Multidisciplinary Optimization 63 (2021) 2101–2123. URL: https://doi.org/10.1007%2Fs00158-020-02806-x. doi:10.1007/s00158-020-02806-x.

[47] B. S. Lazarov and O. Sigmund, Filters in topology optimization based on Helmholtz-type differential equations, International Journal for Numerical Methods in Engineering 86 (2010) 765–781.

[48] D. Arnold, F. Brezzi and M. Fortin, A stable finite element method for the Stokes equations, Calcolo 21 (1984) 337–344.

[49] T. Schwedes et al, Mesh dependence in PDE-constrained optimisation – An Application in Tidal Turbine Array Layouts, 1 ed., Springer, 2017.

[50] COMSOL, CFD Module User's Guide, 5.4, COMSOL, 2018.

[51] CFD Online, Turbulence length scale, 2020. URL: https://www.cfd-online.com/Wiki/Turbulence_length_scale.

[52] G. Pavesi, Impeller Volute and Diffuser Interaction. In Design and Analysis of High Speed Pumps, Educational Notes RTO-

EN-AVT-143 (2011) 6–1–6–28. URL: http://www.rto.nato.int/abstracts.asp.

[53] L. F. Sá et al, Topology optimization of turbulent rotating flows using Spalart–Allmaras model, Computer Methods in Applied Mechanics and Engineering 373 (2021) 113551. URL: http://www.sciencedirect.com/science/article/pii/S0045782520307362. doi:https://doi.org/10.1016/j.cma.2020.113551.

[54] J. N. Reddy and D. K. Gartling, The finite element method in heat transfer and fluid dynamics, 3 ed., CRC press, 2010.

[55] W. M. Lai et al, Introduction to continuum mechanics, Butterworth-Heinemann, 2009.

[56] CFD group at Washington University in St. Louis, WrayAgarwalModels, 2020. URL: https://github.com/xuhanwustl/WrayAgarwalModels.

Appendix A. Alternative unified objective function

From eq. (18), by considering the weak form of the Navier-Stokes equations with the velocity $\boldsymbol{v}_{\text{abs}}$ (or $\boldsymbol{v}$) being considered instead of $\boldsymbol{w}_v$, it is possible to represent all of the objective functions as part of a single objective function with internal weights:

$$
\begin{aligned}
J = {} & w_\Phi w_{H,r} w_{H,rs} \int_{\Omega_r} \left[\frac{1}{2}(\mu + \mu_{\text{T}})(\nabla \boldsymbol{v}_{\text{abs}} + \nabla \boldsymbol{v}_{\text{abs}}{}^T) \bullet \right. \\
& \left. (\nabla \boldsymbol{v}_{\text{abs}} + \nabla \boldsymbol{v}_{\text{abs}}{}^T) \right] d\Omega_r \\
& + w_\Phi w_{H,rs} w_{p,s} \int_{\Omega_s} \left[\frac{1}{2}(\mu + \mu_{\text{T}})(\nabla \boldsymbol{v}_{\text{abs}} + \nabla \boldsymbol{v}_{\text{abs}}{}^T) \bullet \right. \\
& \left. (\nabla \boldsymbol{v}_{\text{abs}} + \nabla \boldsymbol{v}_{\text{abs}}{}^T) \right] d\Omega_s \\
& - w_\Phi w_{H,r} w_{H,rs} \int_{\Omega_r} \boldsymbol{f}_{r,r}(\alpha) \bullet (\boldsymbol{v}_{\text{abs}} - \boldsymbol{\omega} \wedge \boldsymbol{r}) d\Omega_r \\
& - w_{H,rs} \int_{\Omega_r} \boldsymbol{f}_{r,r}(\alpha) \bullet (\boldsymbol{\omega} \wedge \boldsymbol{r}) d\Omega_r \\
& - w_\Phi w_{H,rs} w_{p,s} \int_{\Omega_s} \boldsymbol{f}_{r,s}(\alpha) \bullet \boldsymbol{v}_{\text{abs}} d\Omega_s \\
& + w_\Phi w_{H,r} w_{H,rs} \int_{\Omega_r} [2\rho(\boldsymbol{\omega} \wedge (\boldsymbol{v}_{\text{abs}} - \boldsymbol{\omega} \wedge \boldsymbol{r})) \\
& + \rho \boldsymbol{\omega} \wedge (\boldsymbol{\omega} \wedge \boldsymbol{r})] \bullet (\boldsymbol{v}_{\text{abs}} - \boldsymbol{\omega} \wedge \boldsymbol{r}) d\Omega_r \\
& - w_{H,r} w_{H,rs} \int_{\Omega_r} \nabla \bullet [(\mu + \mu_{\text{T}})(\nabla \boldsymbol{v}_{\text{abs}} + \nabla \boldsymbol{v}_{\text{abs}}{}^T)] d\Omega_r \\
& - w_{H,rs} w_{p,s} \int_{\Omega_s} \nabla \bullet [(\mu + \mu_{\text{T}})(\nabla \boldsymbol{v}_{\text{abs}} + \nabla \boldsymbol{v}_{\text{abs}}{}^T)] d\Omega_s \\
& + w_{p,s} \int_{\Omega_s} \frac{1}{2} \nabla \bullet (\rho \boldsymbol{v}_{\text{abs}} (\boldsymbol{v}_{\text{abs}} \bullet \boldsymbol{v}_{\text{abs}})) d\Omega_s
\end{aligned}
\tag{A.1}
$$

where the dimensionless weights w_Φ, $w_{H,r}$, $w_{p,s}$ and $w_{H,rs}$ should be set as non-zero. If the weights are set in a *summation* fashion in all terms – for example, for the first term, it would be $(w_\Phi + w_{H,r} + w_{H,rs})$ instead of $w_\Phi w_{H,r} w_{H,rs}$, the weights are allowed to be set as zero as well, and the final form of the equations would be similar to considering eq. (18), without, however, the need of scaling the objective functions, due to using the same measurement units.

Note that eq. (A.1) is quite complex, featuring intricate intermixed dependencies which may cloud the physical meaning of each term when trying to attain a certain improvement, including possibly making the choice of weights harder. Also, there is a second order derivative in the velocity in the penultimate and antepenultimate terms of eq. (A.1), which may be an issue depending of the numerical method being considered. Thus, for more clarity for the physical meanings and to avoid the mentioned issue in the numerical method, eq. (18) is considered.

Appendix B. Finite element formulation for MRF under polar coordinates

The weak form of the problem defined for polar coordinates ($\boldsymbol{s}_c = (r, \theta)$) depends on the weighted-residual and the Galerkin methods for the velocity-pressure (mixed) formulation [54], and relies on converting the differential operators to polar coordinates, as well as converting the integrals. Thus, the weak form of the problem becomes:

$$
\begin{aligned}
&F = R_c + R_m + R_{\mathrm{WA2018}} = 0,\\
&R_c = \int_{\Omega_c} [\nabla \bullet \boldsymbol{v}_{\mathrm{abs}}] w_p r d\Omega_c,\\
&R_m = \int_{\Omega_c} [\rho \nabla \boldsymbol{v}_{\mathrm{abs}} \bullet \boldsymbol{v}_{\mathrm{abs}}] r d\Omega_c\\
&+ \int_{\Omega_{c,r}} [-\rho \nabla \boldsymbol{v}_{\mathrm{abs}} \bullet (\boldsymbol{\omega} \wedge \boldsymbol{r}) - \rho \nabla (\boldsymbol{\omega} \wedge \boldsymbol{r}) \bullet (\boldsymbol{v}_{\mathrm{abs}} - \boldsymbol{\omega} \wedge \boldsymbol{r})\\
&+ \rho 2\boldsymbol{\omega} \wedge (\boldsymbol{v}_{\mathrm{abs}} - \boldsymbol{\omega} \wedge \boldsymbol{r}) + \rho \boldsymbol{\omega} \wedge (\boldsymbol{\omega} \wedge \boldsymbol{r})] \bullet \boldsymbol{w}_v r d\Omega_{c,r}\\
&- \int_{\Omega_c} \rho \boldsymbol{f} \bullet \boldsymbol{w}_v r d\Omega_c + \int_{\Omega_c} (\boldsymbol{T} + \boldsymbol{T}_R) \bullet (\nabla \boldsymbol{w}_v) r d\Omega_c\\
&- \oint_{\Gamma_c} [(\boldsymbol{T} + \boldsymbol{T}_R) \bullet \boldsymbol{w}_v] \bullet \boldsymbol{n} r d\Gamma_c + \int_{\Omega_c} \kappa(\alpha) \boldsymbol{v}_{\mathrm{mat,rs}} \bullet \boldsymbol{w}_v r d\Omega, \text{ and}\\
&R_{\mathrm{WA2018}} = \int_{\Omega_{c,s}} [\rho \boldsymbol{v}_{\mathrm{abs}} \bullet \nabla R_{\mathrm{T}}]\, w_{R_{\mathrm{T}}} r d\Omega_{c,s}\\
&+ \int_{\Omega_{c,r}} [\rho (\boldsymbol{v}_{\mathrm{abs}} - \boldsymbol{\omega} \wedge \boldsymbol{r}) \bullet \nabla R_{\mathrm{T}}]\, w_{R_{\mathrm{T}}} r d\Omega_{c,r}\\
&+ \int_{\Omega_c} [(\sigma_R \rho R_{\mathrm{T}} + \mu) \nabla R_{\mathrm{T}}] \bullet \nabla w_{R_{\mathrm{T}}} r d\Omega_c\\
&- \oint_{\Gamma_c} \boldsymbol{n} \bullet [(\sigma_R \rho R_{\mathrm{T}} + \mu) \nabla R_{\mathrm{T}}] w_{R_{\mathrm{T}}} r d\Gamma_c\\
&- \int_{\Omega_c} \rho C_1 R_{\mathrm{T}} S w_{R_{\mathrm{T}}} r d\Omega_c\\
&- \int_{\Omega_c} f_1 C_{1,k\text{-}\omega} \rho \frac{R_{\mathrm{T}}}{S} \nabla R_{\mathrm{T}} \bullet \nabla S w_{R_{\mathrm{T}}} r d\Omega_c\\
&+ \int_{\Omega_c} \rho (1 - f_1) \min \left[C_{2,k\text{-}\varepsilon} R_{\mathrm{T}}^2 \left(\frac{\nabla S \bullet \nabla S}{S^2} \right), \right.\\
&\qquad \left. C_m \nabla R_{\mathrm{T}} \bullet \nabla R_{\mathrm{T}} \right] w_{R_{\mathrm{T}}} r d\Omega_c\\
&+ \int_{\Omega_c} \lambda_{R_{\mathrm{T}}} \kappa(\alpha) R_{\mathrm{T}} w_{R_{\mathrm{T}}} r d\Omega_c,
\end{aligned}
\tag{B.1}
$$

where F is the weak form, and R_c, R_m and R_{WA2018} are the residuals of the continuity equation, the linear momentum (Navier-Stokes) equations, and the Wray-Agarwal (2018) equation. The polar integration domains correspond to the same ones presented in previous sections (Ω, Ω_s, Ω_r , and Γ) but converted to polar coordinates: The resulting polar domains are indicated by the additional subscript c and are equal to their counterparts multiplied by r, as Ω_c , $\Omega_{c,s}$, $\Omega_{c,r}$, and Γ_c, respectively. The test functions for each state variable ($\boldsymbol{v}_{\mathrm{abs}}$, p, R_T) are given as $\boldsymbol{w}_v$, $\boldsymbol{w}_p$, and $\boldsymbol{w}_{R_{\mathrm{T}}}$, respectively. Eq. (B.1) can also be extended to cylindrical coordinates ($\boldsymbol{s}_c = (r, \theta, z)$). Note that the differential operators, such as gradient and divergence, are expressed differently depending on the coordinate system being considered [55].

Appendix C. Pseudocode of the implementation

All the information in the article is sufficient for the reproduction of this article. Particularly, the original TOBS implementation can be obtained from Souza et al. [32] and then adjusted for this work. The FEniCS and OpenFOAM® softwares are open source, as well as the FEniCS TopOpt Foam library [37], which also provides an example of usage (sample code). The implementation in FEniCS is then straightforward from the provided weak forms in this work, because it uses a high-level description for the variational formulation (UFL). In the case of considering polar coordinates, the differential operators ("`grad`", "`curl`", "`div`") must be programmed by hand by using the "`Dx(var,component_num)`" or "`var.dx(component_num)`" functions, because the operators provided by FEniCS assume Cartesian coordinates.

The part of the implementation that is performed in OpenFOAM® , consists of including the inverse permeability term in the "`simpleFoam`" solver from OpenFOAM® , which is already able to take MRF into account (already available in the git repository from Alonso et al. [37], as "`CustomSimpleFoam`"), and also in the Wray-Agarwal (2018) turbulence model, which needs to be adjusted from the original git repository [56] according to eq. (7) considering $f_{\mathrm{MRF}} = 0$, because OpenFOAM® can internally change the fluxes in order to take MRF into account.

In order to facilitate the reproduction of results, a pseudocode is represented in Algorithm 1, where the main FEniCS/dolfin-adjoint functions being used are given between parentheses.

Algorithm 1 Pseudocode of the implementation

Input parameters: Flow rate, turbulence, dimensions, optimization parameters and constants.
Result: Optimized topology (optimized distribution of the design variable) and its post-processed simulation.
1 [FEniCS] Generate the mesh using Gmsh [43], import it in FEniCS and convert it to polar coordinates.
2 [FEniCS] Prepare the state variables and the design variable (pseudo-density) (MINI element (velocity and pressure) ("`FiniteElement`", "`VectorElement`", "`NodalEnrichedElement`"), CG1 "`FiniteElement`" (pseudo-density, undamped turbulent viscosity), "`MixedElement`" (for pressure, velocity and undamped turbulent viscosity), "`FunctionSpace`"), by considering periodic boundaries.
3 [FEniCS] Define the Dirichlet boundary conditions (see eq. (9)) ("`DirichletBC`"), and leave the boundaries marked by a "`MeshFunction`".
4 [FEniCS] Define the initial guess of the topology (i.e., the initial values of the design variable) ("`interpolate`").
5 [FEniCS] Define the material model for the inverse permeability (eq. (12)).
6 [FEniCS] Compute the Helmholtz pseudo-density filter.
7 [FEniCS] Define the weak form of the fluid flow problem (eq. (B.1)) by using the filtered design variable.
8 [OpenFOAM®] Prepare the default OpenFOAM® setup dictionaries, the material model properties ("`materialmodelProperties`"), as well as the MRF setup ("`topoSetDict`" and "`MRFProperties`").
9 [FEniCS → OpenFOAM®] Convert the mesh and boundary markings from FEniCS to OpenFOAM® by using FEniCS TopOpt Foam [37].
10 Start the topology optimization iterations, until convergence. This part may be implemented manually, or by an optimization solver based on the dolfin-adjoint built-in "`IPOPTSolver`". In the first case, the implementation framework should be similar to [32]; in the second case, the implementation framework should be similar to [37]. All of the operations performed with FEniCS TopOpt Foam are available in the sample code from [37]. Exemplifying for the first case,
9.1 [FEniCS] Compute the Helmholtz pseudo-density filter without annotations ("`annotate = False`"), and update the filtered design variable values.
9.2 [FEniCS] Map the variables from the polar coordinates to the Cartesian coordinates.
9.3 [FEniCS → OpenFOAM®] Map the current state variables and the filtered design variable to OpenFOAM® , by using the FEniCS TopOpt Foam library.
9.4 [OpenFOAM®] Solve the simulation in OpenFOAM® .
9.5 [OpenFOAM® → FEniCS] Map the current state variables to FEniCS, by using the FEniCS TopOpt Foam library
9.6 [FEniCS] Map the variables from the Cartesian coordinates to the polar coordinates.
9.7 [dolfin-adjoint] Compute the sensitivities by using dolfin-adjoint: first, use the "`pyadjoint`" module from dolfin-adjoint in order to temporarily stop annotations, and then compute the sensitivities ("`compute_gradient`").
9.8 [TOBS] Define and solve the TOBS step.
9.9 [FEniCS] Update the design variable.
9.10 [TOBS] Check for convergence.
10 Post-process the optimized topology.
11 Set up the simulation for OpenFOAM® in the post-processed mesh, and solve it.